NONLINEAR MICROWAVE INTERACTIONS WITH VOLTAGE-GATED GRAPHENE DEVICES

A Dissertation

Presented to

The Graduate Faculty of The University of Akron

In Partial Fulfillment

of the Requirements for the Degree

Doctor of Philosophy

Michael Robert Gasper

July, 2020

NONLINEAR MICROWAVE INTERACTIONS WITH VOLTAGE-GATED GRAPHENE DEVICES

Michael Robert Gasper

Dissertation

Approved:

Advisor
Dr. Ryan C. Toonen

Committee Member
Dr. Kye-Shin Lee

Committee Member
Dr. Igor Tsukerman

Committee Member
Dr. Alper Buldum

Committee Member
Dr. Ben Yu-Kuang Hu

Accepted:

Department Chair
Dr. Robert Veillette

Interim Dean of the College
Dr. Craig Menzemer

Acting Dean of the Graduate School
Dr. Marnie Saunders

Date

ABSTRACT

In this dissertaton, methods of fabrication and testing micro- and nano-scaled thermoelectric microwave power detectors based on graphene are explored. Initial detectors show sensitivities of 0.87 mV/mW and each chapter herein decribes the iterations and improvements made to the devices. In the end, detectors have shown sensitivities of up to 60.25 mV/mW when accounting for the reflection coefficient of the device, over a 690% increase in sensitivity. Commercially-available detectors that feature zero DC power consumption and operate over similar frequency ranges typically offer a power detection sensitivity of 500 mV/mW. However, state-of-the-art thermoelectric detectors based on CMOS and MEMS technologies offer power detection sensitivities that are typically lower than 0.4 mV/mW. Unoptimized graphene based detectors have been shown to outperform CMOS and MEMS detectors. An outlook is provided on further optimizations that can be made to the devices.

ACKNOWLEDGEMENTS

I would first and foremost like to thank my advisor Dr. Ryan C. Toonen for his support and insight during my graduate studies. I would like to sincerely thank my committee members Dr. Kye-Shin Lee, Dr. Igor Tsukerman, Dr. Alper Buldum, and Dr. Ben Yu-Kuang Hu for their support and guidance through this whole process. I would also like to thank my friend and colleague in the Zips Electronic Nanotechnology Lab (ZEN-LAB) Dr. Nitin Parsa for his help, support, and just being there to talk. I would like to thank my friends and colleagues at NASA Glenn Research Center Nick Varaljay, Dr. Bob Romanofsky, and Dr. Felix Miranda for their help and support for fabrication and experiments. Finally, I would like to thank my wife Catherine for helping me stay positive when research wasn't going my way. Everyone has been essential to me during my studies in one way or another.

TABLE OF CONTENTS

LIST OF FIGURES

CHAPTER I

INTRODUCTION

Graphene, a single atom layer of carbon, has high carrier mobility and is of great interest in radio frequency and microwave applications. The chemical vapor deposition (CVD) technique for synthesizing graphene is relatively inexpensive, allows for large-scale production, and enables graphene to be transferred to a variety of microwave-compatible substrates. This research focuses on the use of Graphene as a detection medium for microwave signals. Work has been done on the fabrication and testing of basic devices. Care must be taken in order to fabricate structures without significantly disturbing the graphene layer. Power detection has been shown for frequencies up to approximately 3 GHz on both micro and nano electronics structures, with sensitivities as high as 60.25 mV/mW.

1.1 Motivation

The motivation for this work is the detection of low level microwave signals down to the single photon. Single photon detection is limited by background noise. The one-sided noise power spectral density of blackbody noise is given by

$$\frac{N_0}{BW} = \frac{2hf}{e^{hf/k_BT} - 1}. \tag{1.1}$$

The noise power per unit bandwidth of the cosmic microwave background radiation (CMBR) is calculated using Eqn. 1.1 at a temperature of $T = 2.7$ K, k_B =Boltzmann's Constant, and h =Planck's Constant as a function of f =frequency, setting a lower limit on the noise that a detector may face. The CMBR at 2.7 K, the backgroound temperature of space, sets the noise floor for a minimum detectable signal. The CMBR energy intersects the energy of single photon energy,

$$E = hf, \tag{1.2}$$

at a frequency of approximately 61.8 GHz, Fig. 1.1 [1]. Thus a fundamental limit of single photon detection is shown at microwave frequencies within the V-band, 40-75 GHz.

1.2 Why Graphene?

Graphene is a two-dimensional allotrope of carbon. It is a single layer of carbon atoms arranged in a hexagonal lattice, Fig. 1.2. Its unique band structure gives it electrical properties that have led to new types of micro and nano-electronic devices [2]. It is a semi-metal and it may be doped either chemically or electrically to alter carrier concentrations [3]. The goal of this research is to use these properties of graphene to construct mircrowave power detectors. Steps are taken to fabricate such devices without significantly altering the properties of the graphene. Hydrocarbons introduced during processing degrade the desirable properties of the graphene, making fabrication of any electronic structures difficult. Many processes will either damage

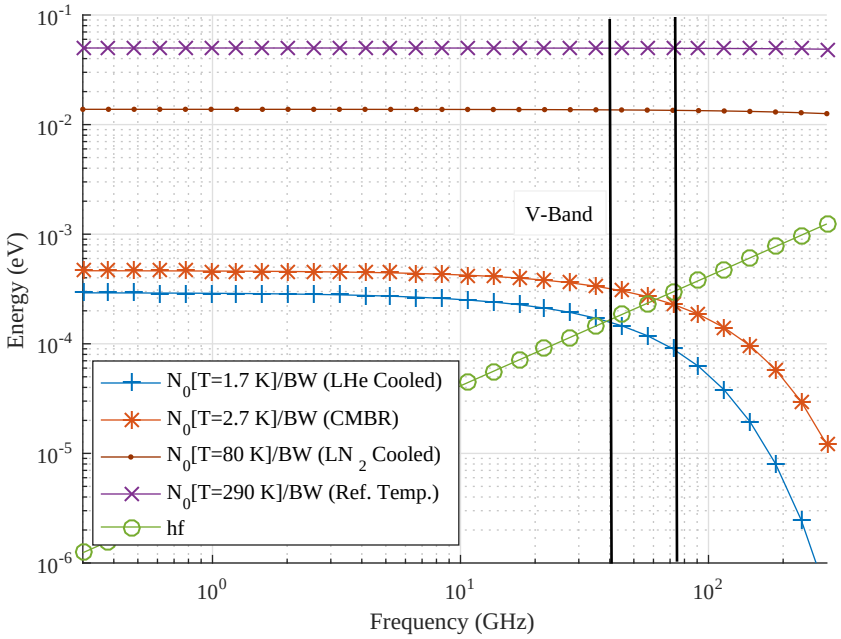

Figure 1.1: Noise power per unit bandwidth at various temperatures. The energy of a single photon intersects that of the CMBR in the microwave V-band.

or unintentionally dope the material. Raman spectroscopy is used to determine the quality of graphene by revealing the number of layers and defects. The Raman spectrum, Fig. 1.3, displays three peaks of interest. The intensity of the G' band (2D, stacking order, 2690 cm^{-1}) peak is greater than the G (in-plane vibration of sp^2 carbon atoms, 1580 cm^{-1}) peak in monolayer graphene. As the number of layers of graphene increases (bilayer and beyond), the intensity of the G' band peak becomes less than the G peak. The Raman spectrum may also reveal a D band peak (1350 cm^{-1}). This peak represents disordered carbon and is introduced due to handling and processing of graphene samples, breaking the hexagonal crystal structure [5, 6].

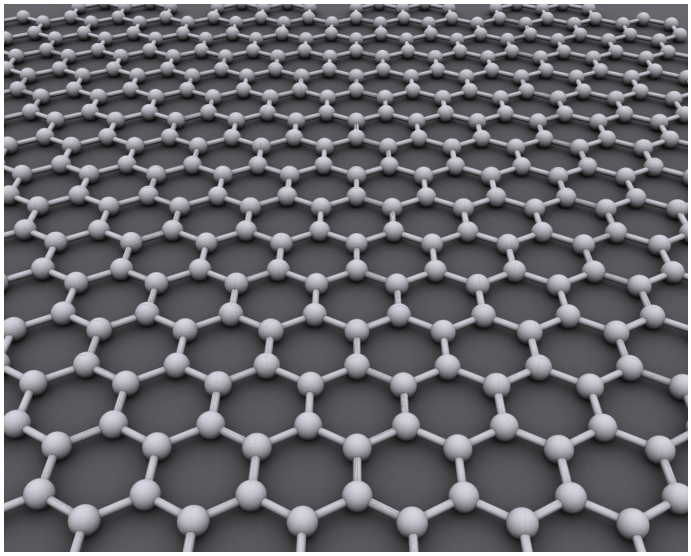

Figure 1.2: Illustration of the hexagonal lattice of graphene [4].

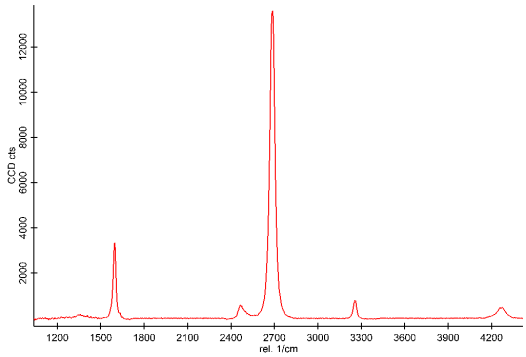

Figure 1.3: Typical Raman spectrum of CVD grown graphene from Graphenea [7] showing the G and G' peaks at 1580 cm^{-1} and 2690 cm^{-1} respectively.

In pristine single layer graphene, the tight binding model Hamiltonian leads to the derived energy bands

$$E_{\pm} = \pm t\sqrt{3 + f(k)} - t' f(k), \tag{1.3}$$

where

$$f(k) = 2\cos\left(\sqrt{3}k_y a\right) + 4\cos\left(\frac{\sqrt{3}}{2}k_y a\right)\cos\left(\frac{3}{2}k_x a\right) \tag{1.4}$$

and $t = 2.7$ eV and $t' = -0.2t$ represent the nearest-neighbor hopping energy and next nearest-neighbor hopping energy respectively. The value a in Eq. 1.4 is the nearest neighbor separation distance between carbon atoms. These energy bands meet at a set of discrete points, referred to as the Dirac points, Fig. 1.4. The Dirac points and the Dirac Cone band structures occur at and around the K and K' points in the corners of the graphene Brillouin Zone. Electrons around this point act as massless Dirac Fermions [8], with effective carrier velocities approaching the speed of light. Graphene's physical performance exceeds that of conventional materials in that it displays high electron mobility at room temperature, the ability to sustain high current densities, it is impermeable to gases, and has a high thermal conductivity [9]. These properties are only achieved with high quality graphene samples, usually fabricated via mechanical exfoliation. However only small flakes of graphene can be gathered by this method. Newer methods of fabricating graphene have been developed and high quality samples are now readily available.

Graphene was chosen as the material of interest in this work for it properties described above. The band structure of graphene gives it unique electronic properties that can be used for a variety of applications. The graphene used in this work is commercially available chemical vapor deposition (CVD) grown graphene, purchased from Graphenea. The properties of these graphene samples are 97% transparency, 98% wafer coverage, monolayer with a theoretical thickness 0.345 nm, FET electron

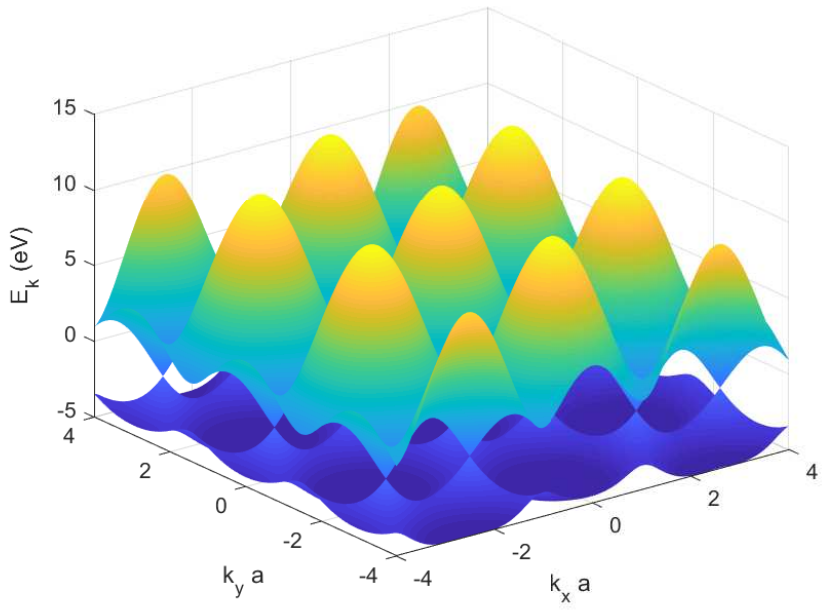

Figure 1.4: Electronic dispersion in the graphene lattice. Derivation found in [8]. The areas on the band-structure diagram around where the light blue sections meet with the dark blue sections, $E_K = 0$, are the Dirac cones. The locations where the Dirac cones meet, the K and K' points, are known as the Dirac points.

mobility on Al_2O_3 passivated SiO_2/Si of 6900 cm^2/Vs [10], and FET electron mobility on SiO_2/Si: 3760 cm^2/Vs [11], Sheet Resistance on SiO_2/Si of 450±40 Ω/sq (1 cm × 1 cm), Grain sizes up to 20 μm, and Raman Spectroscopy on each batch where I(G)/I(2D)<0.7; I(D)/I(G)<0.05 [7].

1.3 Organization of Dissertation

This work starts with a background on basic concepts considered throughout the dissertation in Chapter 2. Initial attempts to fabricate graphene microstructures are in Chapter 3, where device performance is investigated via characterization at DC along with power detection measurements at 433.92 MHz. Device qualtity was degraded during processing and new, improved, devices were then fabricated in Chapter 4. These devices have shown improved performance, however, the physical detection mechanims remain obscurred. Nanostructures are then discussed in Chapter 5, where nanofabrication continues directly from the end of the microfabrication process. Chapter 6 then discusses graphene nano-constriction devices where the detection mechanism is observed to be the thermoelectric effect. The graphene nanoconstrictions show a poor reflection coefficient, hampering the detection capabilities of the devices. Chapther 7 discusses the development and fabrication of co-planar waveguide resonators used to more efficiently deliver power to the graphene nanocontriction elements. Also considered, in Chapter 8, is a side project done in collaboration with NASA Glenn Research Center to create graphene frequency multipliers that can withstand harsh environments. Finally, a summary and the conclusions of this work are presented in Chapter 9

CHAPTER II

BACKGROUND

This chapter serves offers a brief introduction to the topics presented in this dissertation. Concepts, design equations, and definitions are presented that are used throughout this work.

2.1 Graphene Band Structure

The band structure of graphene can be derived with the tight-binding model. In the tight binding model electrons can move to nearest (and next nearest) neighbor sites in the atomic lattice. Carbon has 4 valence electrons which form sp^2 hybridized orbitals in graphene. The σ bonds in graphene are tightly bound and there are two weak π bonds that can be formed with nearest neighbor atoms. The tight binding model considering up to third nearest neighbor hopping can give accurate results over the entire Brillouin Zone [12]. We will examine only first nearest neighbors here to simply illustrate the point.

The Hamiltonian for nearest neighbor hopping is given in position space by

$$H = -t \sum_{i,j} c_i^\dagger c_j \tag{2.1}$$

where $c_i^\dagger c_j$ represents the the annihilation of a fermion in state j and the creation of one in state i. The creation and annihilation operators can be used to calculate the wave function of state i, ψ_i, in terms of the wave function in state j, ψ_j, giving $\psi_i = c_i^\dagger c_j \psi_j$. We are only considering hopping between nearest neighbors B at points i with initial state A at point j such that $i = 1, 2, 3$ and $j = 1$ in this case. Now we have

$$H\psi = E\psi. \tag{2.2}$$

So for A and and its three nearest B lattice neighbors we obtain

$$-t(c_{B,1}^\dagger c_A \psi_A + c_{B,2}^\dagger c_A \psi_A + c_{B,3}^\dagger c_A \psi_A) = E\psi_A, \tag{2.3}$$

which simplifies to

$$-t(\psi_{B,1} + \psi_{B,2} + \psi_{B,3}) = E\psi_A. \tag{2.4}$$

Assuming the solution to the wavefunction is of the form

$$\psi = \begin{cases} \psi_A e^{j\mathbf{k}\cdot\mathbf{r}} & \text{for an electron in state A} \\ \psi_B e^{j\mathbf{k}\cdot\mathbf{r}} & \text{for an electron in state B} \end{cases} \tag{2.5}$$

and substituting it into Eq. 2.4 along with the displacement vectors of the $i = 1, 2, 3$ B atoms with respect the A atom we finally get

$$-t[e^{-jk_y a} + 2e^{jk_y \frac{a}{2}} \cos\left(\sqrt{3}\frac{a}{2}k_x\right)] \mid \psi_B \mid = E\psi_A \tag{2.6}$$

and similarly for a particle entering state A from B

$$-t[e^{jk_y a} + 2e^{-jk_y \frac{a}{2}} \cos\left(\sqrt{3}\frac{a}{2}k_x\right)] \mid \psi_A \mid = E\psi_B. \tag{2.7}$$

Equations 2.6 and 2.7 can be written as an eigenvector equation of a 2×2 matrix, which has eigenvalues

$$E = \pm t\sqrt{3 + 2\cos\left(\sqrt{3}k_x a\right) + 4\cos\left(\frac{\sqrt{3}}{2}k_x a\right)\cos\left(\frac{3}{2}k_y a\right)}. \tag{2.8}$$

This solution differs from the solution shown in Chapter 1 in that Eq. 1.3 contains a term to account for second nearest neighbor hopping.

2.2 Microwave Structures

2.2.1 Corbino Discs

Corbino discs are the main structures of interest in this work. They used for experiments because they are easy to probe and their symmetry makes for simple calculations. A Corbino disc is a structure with a circular inner contact surrounded by an annular outer contact, Fig. 2.1. It is easily thought of as a short section of terminated coaxial cable.

A Corbino disc has an electric field that radiates radially between its contacts, thus a current between the contacts will also flow radially. In the presence of a magnetic field the current is deflected, similar to a Hall bar. However, unlike a Hall bar, there are no edges in the geometry for charge to accumulate. The Corbino disc is like a Hall bar without the associated Hall voltage. The trajectory of the deflected electrons within the disc is like a spiral, or water going down a drain, as shown in Fig. 2.2 [13]. As a result of the longer electron path, the resistance of the disc increases

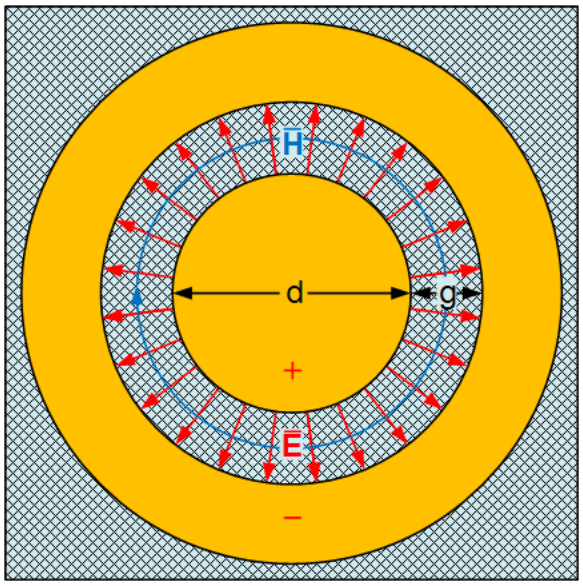

Figure 2.1: Corbino disc structure.

as described by

$$R = R_0(1 + \mu^2 B^2) \tag{2.9}$$

where μ is the mobility and B is the applied magnetic field.

An advantage of using the Corbino disc in material characterization is the symmetry of the device. The symmetry of the Corbino disc allows for simple calculations and material parameter extraction [14]. Starting with the reflection coefficient (S_{11}) and characteristic impedance (Z_0=50Ω), the load impedance is found as

$$Z_L = Z_0 \frac{1 + S_{11}}{1 - S_{11}} \tag{2.10}$$

and used to find the relative permittivity of the sample

$$\epsilon = \frac{1}{j\omega Z_L C_0}. \tag{2.11}$$

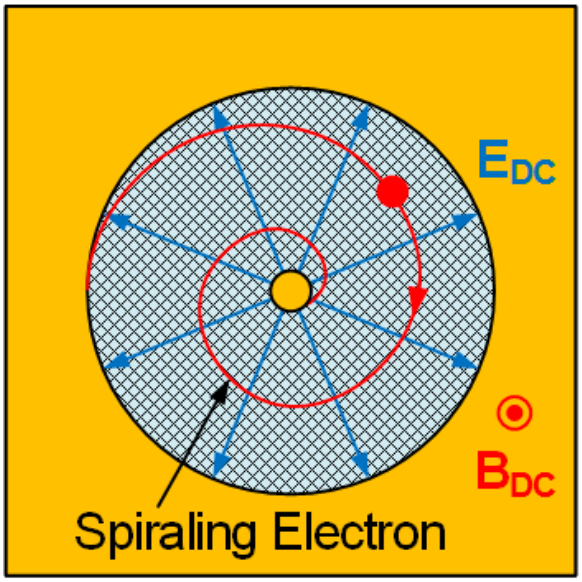

Figure 2.2: The Corbino effect.

The variable C_0 is the free space capacitance of the Corbino disc and is calculated as

$$C_0 = \frac{2\pi\epsilon_0 h}{\ln\left(\frac{d+2g}{d}\right)}. \tag{2.12}$$

The permittivity is a complex number and can be expressed in terms of its real and imaginary components

$$\epsilon = \epsilon' + j\epsilon'', \tag{2.13}$$

and the imaginary component can be rewritten in terms of conductivity and frequency as

$$\epsilon'' = \frac{\sigma'}{\omega}. \tag{2.14}$$

The loss tangent of the material is expressed using the components of the complex permittivity and conductivity as

$$\tan\delta = \frac{\epsilon''}{\epsilon'} \tag{2.15}$$

and

$$\tan\delta = \frac{\sigma'}{\omega\epsilon'}. \tag{2.16}$$

The imaginary component of the complex conductivity can then be defined as

$$\omega\epsilon' = \sigma'' \tag{2.17}$$

and the complex conductivity is

$$\sigma = \sigma' + j\sigma''. \tag{2.18}$$

The attenuation constant and the phase constant are expressed as

$$\alpha = \sqrt{\mu_0\omega\sigma''}\Big(\frac{1}{2}\Big[\sqrt{1+(\frac{\sigma'}{\sigma''})}-1\Big]\Big)^2 \tag{2.19}$$

and

$$\beta = \sqrt{\mu_0\omega\sigma''}\Big(\frac{1}{2}\Big[\sqrt{1+(\frac{\sigma'}{\sigma''})}+1\Big]\Big)^2 \tag{2.20}$$

respectively. The skin depth is simply the inverse of the attenuation constant. The sheet resistance is

$$R_{sh} = \frac{1}{\sigma' h}. \tag{2.21}$$

Thus, using the Corbino disc device structure one can quickly determine a number of material parameters from a simple reflection measurement.

2.2.2 Coplanar Waveguide

Coplanar waveguide (CPW) is described by center strip width S, gap width W, substrate thickness h, and metal thickness t. The characteristic impedance of a coplanar waveguide is given by

$$Z_0 = \frac{30\pi}{\sqrt{\epsilon_e}} \frac{K(k')}{K(k)} \tag{2.22}$$

and the effective dielectric constant is

$$\epsilon_e = 1 + \frac{\epsilon_r - 1}{2} \frac{K(k')K(k_1)}{K(k)K(k_1')} \tag{2.23}$$

where ϵ_r is the relative dielectric constant of the substrate material [15]. The value $K(k)/K(k')$ is a ratio of elliptic functions of the first kind such that

$$\frac{K(k)}{K(k')} = \begin{cases} \left[\frac{1}{\pi} \ln\left(2\frac{1+\sqrt{k'}}{1-\sqrt{k'}}\right)\right]^{-1} & \text{for } 0 \leq k \leq 0.7 \\ \frac{1}{\pi} \ln\left(2\frac{1+\sqrt{k}}{1-\sqrt{k}}\right) & \text{for } 0.7 \leq k \leq 1 \end{cases} \tag{2.24}$$

where

$$k = \frac{a}{b},\ a = \frac{S}{2},\ b = \frac{S}{2} + W,\ k_1 = \frac{\sinh(\pi a/2h)}{\sinh(\pi b/2h)},\ \text{and } k' = \sqrt{1-k^2}. \tag{2.25}$$

The metal thickness should be at least three skin depths δ_s thick if not up to ideally five when designing CPW structures to minimize losses.

2.3 Basics of Lithography

Photoresists are spin on polymers used in photoligraphy. There are two types of photoresist, positive tone and negative tone. Positive tone resist is weakened when

exposed to light and can be easily removed while negative tone resist is strengthened when exposed to light. The type of photoresist to use depends on the nature of the processing. Image resolution, resist thickness, and exposure method are just some parameters to consider when choosing a resist. Spinning is the application of a photoresist to a substrate. Spinning the substrate at high speeds and then applying resist allows the resist to evenly distribute itself on the substrate. Spinning also helps to drive solvents out of the resist and preps it for exposure. The pre-bake is heating the substrate and resist in order to remove remaining solvents from the resist. If the resist is exposed without removing solvents, then the exposure and subsequent steps may fail. Exposure is subjecting the photoresist to energy in order to harden or weaken the photoresist in specific places. The post-bake step is the heating of the resist after exposure in order to strengthen the effects of the energy exposure. The post-bake is necessary with most negative tone resists. Development is the washing away of areas of weakened photoresist in order to pattern the substrate.

CHAPTER III

GRAPHENE LOADED CORBINO DISCS

Gated graphene has been used to realize a microwave power detector. A Corbino disc structure with Ti/Ag contacts has been fabricated on top of graphene deposited on P-type Si substrates with SiO_2 gate oxides. This device exhibits power detection with a sensitivity reaching 0.87 mV/mW at a frequency of 433.92 MHz using lock-in detection at room temperature. This chapter is has been published in the conference paper "Microwave Power Detection with Gated Graphene" presented at the IEEE International Conference on Nanotechnology in Pittsburgh, PA on July 25-28, 2017 [16].

A simple, single-lithography-mask approach for making detectors that have a Corbino disc geometry with a back gate for modulating channel conductance is discussed. Results from gated microwave power detection experiments where the operating frequency was held at 433.92 MHz, the center of one of the unlicensed industrial, scientific, and medical radio (ISM) bands are also presented.

3.1 Corbino Disc Microfabrication

CVD grown graphene devices were fabricated for use as microwave power detectors. Fig. 3.1 outlines the basic device fabrication process. The process starts by laying

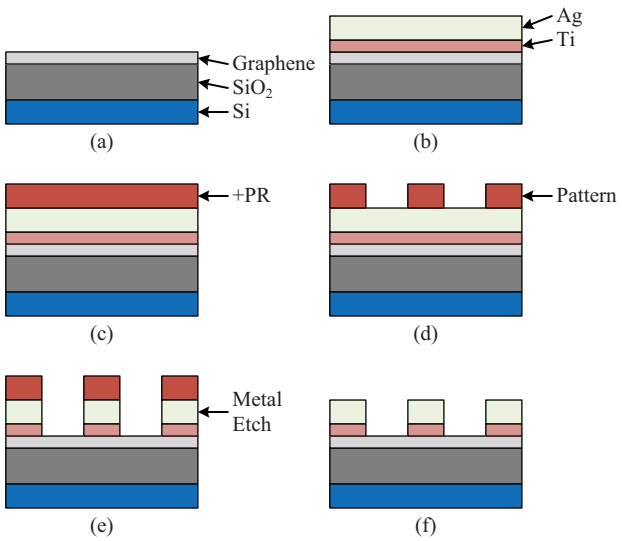

Figure 3.1: (a) Graphene on SiO2 with Si back gate. (b) Metallization of the sample with Ti and Ag. (c) Spin on photoresist. (d) Pattern with negative photomask. (e) Etch away exposed Ag and Ti. (f) Final device structure remains after cleaning residual photoresist.

down a blanket layer of Ti/Ag over the entire substrate. This complete metal covering was used to protect the graphene during photolithographic processing [17]. A 5 nm layer of Ti and 50 nm layer of Ag was deposited via e-beam evaporation. Positive photoresist was then spun on the sample and patterened using a negative photomask. After patterning and development, exposed portions of metal were etched away via a wet etch process and any remaining photoresist was washed away, leaving the desired device structures as shown in Fig. 3.2.

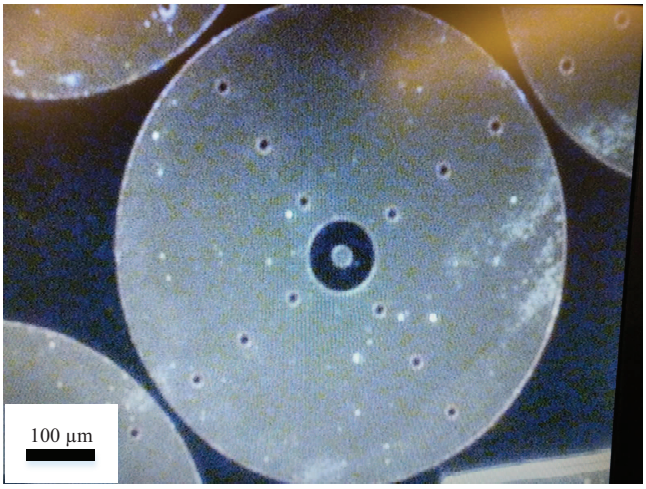

Figure 3.2: Photo of a complete device.

Raman spectrum data was collected on both an unprocessed graphene sample as well as a processed sample with completed device structures. Data from the unprocesed sample, Fig. 3.3, indicates that the graphene is multilayer [5]. While data from the processed sample, Fig. 3.4, shows that the graphene remained intact after the fabrication process. However, some defects were created on the graphene sample as shown by the D band peak ($\sim$1350 cm^{-1}) on the Raman spectrum [18].

I-V traces of device current versus gate voltage for varying bias voltages were collected, as shown in Fig. 3.5. The minimum current is estimated to occur near 150 V, outside the range of available equipment. Annealing future samples could improve device performance and shift the transition point (minimum current) closer to a gate voltage of 0 V [19].

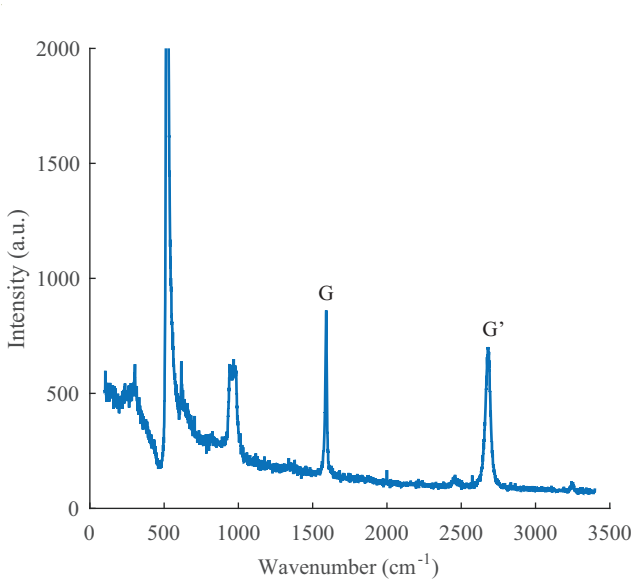

Figure 3.3: Raman spectrum of unprocessed sample displaying G and G' (2D) peaks.

3.2 Power Detection

The graphene structures have been used to realize a microwave power detector operating at 433.92 MHz, in the ISM band. The gated graphene device was illuminated with microwave power chopped at 9.2 kHz. A differential voltage measurement was taken via lock-in detection at the chopping frequency across a 100 kΩ sense resistor, R_S. The sense resistor acted as part of a voltage divider with the device under test [20, 21]. An illustration of the experimental structure is shown in Fig. 3.6 and a photograph of the test setup is shown in Fig. 3.7.

Power detection was characterized at room temperature under vacuum ($<10^{-4}$ Torr) using a Lakeshore Cryotronics CPX-VF probe station with GS-style probes having a ground-to-signal spacing of 250 μm. Power detection data was collected by

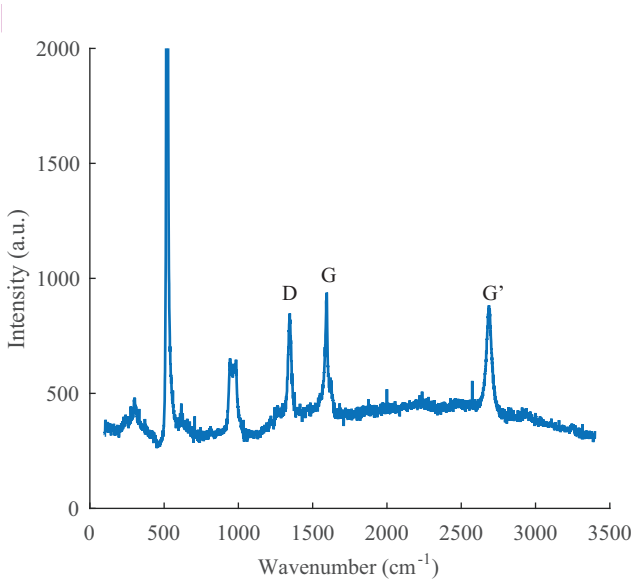

Figure 3.4: Raman spectrum of processed sample displaying G and G' (2D) peaks indicating that the graphene remains on the sample along with some defects, indicated by the D peak.

sweeping the input power (P_{IN}) and measuring the detected signal (V_M) with 0 V gate voltage (V_{GATE}) applied, Fig. 3.8. The graphene Corbino disc detector, with an inner diameter of 60 μm and gap length of 10 μm, achieved a peak sensitivity (S_V) of approximately 0.87 mV/mW and 1 dB roll-off occuring at $P_{IN,1dB} = 4$ dBm, determined via a fit to the measured data with

$$V_M(\text{dBmV}) = b(\text{dB}) + 2P_{IN}(\text{dBm}), \tag{3.1}$$

where S_V (mV/mW) can be obtained from the log-log plot intercept b (dB) from the relation

$$S_V(\text{mV/mW}) = 10^{\frac{b(\text{dB})}{20\text{dB}}} \left(\frac{1\,\text{mW}}{1\,\text{mV}}\right). \tag{3.2}$$

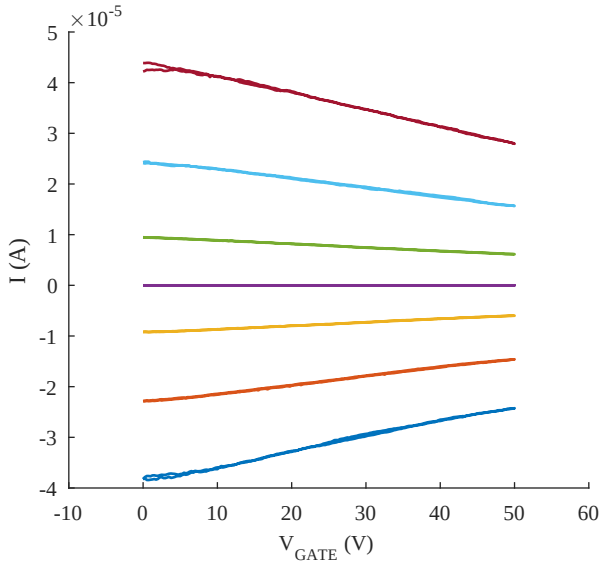

Figure 3.5: Device current vs gate voltage for various applied disc voltages.

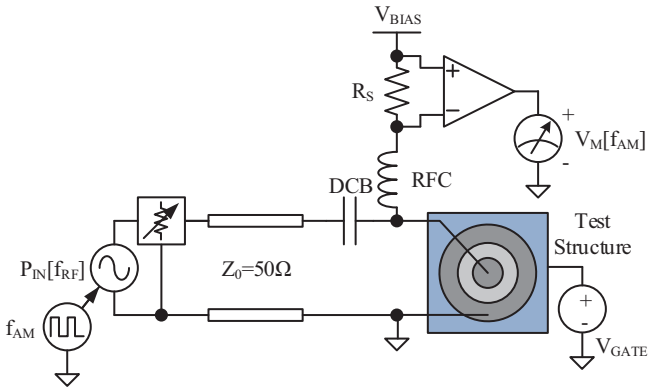

Figure 3.6: Schematic of the graphene power detection circuit.

The graphene detector exceeds the sensitiviy of prevously explored carbon nanotube bolometers at room temperature [20, 21]. Applying a voltage to the gate of the device allows for a small amount of tunability as shown in Fig. 3.9.

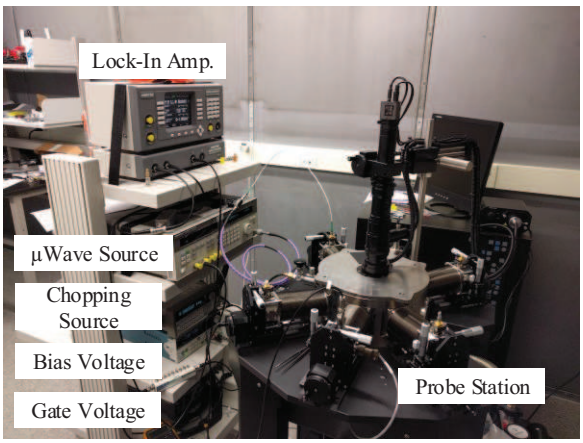

Figure 3.7: Photo of the graphene power detection experimental setup.

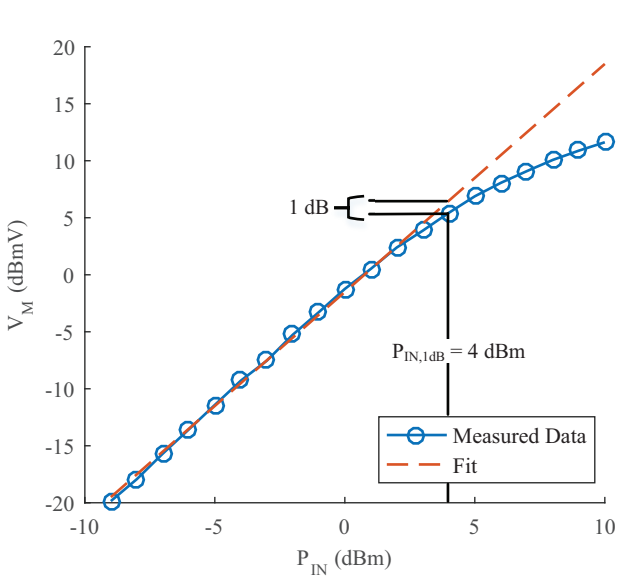

Figure 3.8: Measured voltage vs incident power for 0 V gate voltage.

Measurements taken on additional devices of varying sizes, with inner disc diameters ranging from 40-120 μm and gap lengths ranging from 3-100 μm, displayed sensitivities from 0.156 μV/mW to 0.104 mV/mW. There did not appear to be any

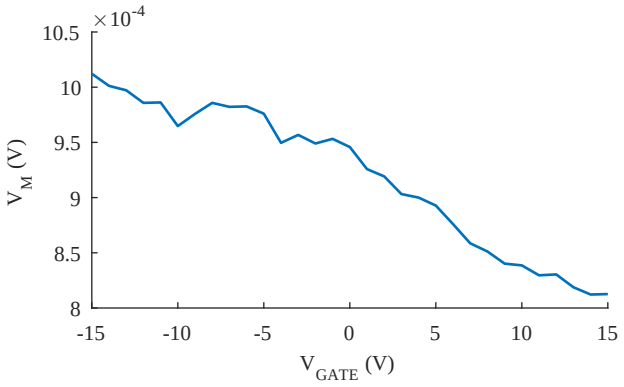

Figure 3.9: Measured voltage vs applied gate voltage for an incident power of 0 dBm.

correlation between the sensitivity of the device and its size in these experiments. It is expected that applying post processing techniques [22] will improve the quality of the graphene detectors.

3.3 Conclusions

Power detection measurements using graphene Corbino discs yielded a peak power sensitivity of 0.87 mV/mW at room temperature. It is expected that the performance can be improved through optimizing the fabrication process and device dimensions as well as lowering the operating temperature. A thicker metal layer will help to increase device yield and prevent damage due to probing. Alterations to the metal etching step can help to improve device yield and graphene quality. The quality of the graphene can be further improved after annealing the devices to remove impurities from the surface. Devices without back gates could help to improve performance at higher

frequencies by removing parasitic capacitances, although at the loss of tunability via the back-gate voltage.

CHAPTER IV

IMPROVED GRAPHENE LOADED CORBINO DISCS

Commercially available, chemical vapor deposition grown, gated graphene has been used to realize microwave power detectors. Corbino disc structures with chrome/gold contacts have been fabricated on top of graphene deposited on P-type silicon substrates with silicon dioxide gate oxides. Devices of varying sizes were used to detect a 433.92 MHz signal, in the ISM band. These test structures exhibited a peak power detection sensitivity of 3.25 mV/mW at 292 K and 5.43 mV/mW at 80 K. The improved graphene detectors exceed the sensitivity of previously reported graphene detectors, 0.86 mV/mW, as well as previously explored carbon nanotube bolometers, 0.36 mV/mW. This chapter has been published in the journal paper "Microwave Power Detection With Voltage-Gated Graphene" in IEEE OPEN JOURNAL ON NANOTECHNOLOGY [23].

4.1 Introduction

Graphene, a single atom layer of carbon in a hexogonal lattice, is of great interest in radio frequency and microwave applications due to its high carrier mobility and DC transfer characteristic [2]. The chemical vapor deposition (CVD) technique for synthesizing graphene is relatively inexpensive, allows for large-scale production, and

enables graphene to be transferred to a variety of microwave-compatible substrates. In this paper, we expand upon previously reported power detection capabilites of graphene loaded Corbino disc test structures [16] and present an improved microwave power detector based on aluminum-oxide passivated monolayer graphene. We also discuss the details involved in our simple, single-lithography-mask approach for making detectors that have a Corbino disc geometry [24] with a back gate for modulating channel conductance [25]. We present the results from gated microwave power detection experiments at both room temperature (292 K) and liquid nitrogen cooled temperature (80 K) where the operating frequency was held at 433.92 MHz, the center of one of the unlicensed industrial, scientific, and medical (ISM) radio bands.

4.2 Device Fabrication

Work has been done in order to improve the previsouly reported device processing method [16]. Fig. 4.1 outlines the Corbino disc test structure fabrication process. The process starts by first cleaning commercially avaliable, CVD-grown monolayer graphene on silicon dioxide/silicon (SiO_2/Si) [7] with rapid thermal annealing (RTA) in forming gas (nitrogen with 4.5% hydrogen) atmosphere at 250 °C for 12 minutes. The RTA helps to reduce impurities absorbed by the graphene surface [7]. Then, a 5 nm sacrificial layer of aluminum was deposited over the entire substrate and allowed to form a native oxide passivation layer. This complete metal covering was used to protect the graphene during photolithographic processing. Negative photoresist (AZ nLOF 2020) was spun on, exposed, and then developed with AZ 300 MIF. The

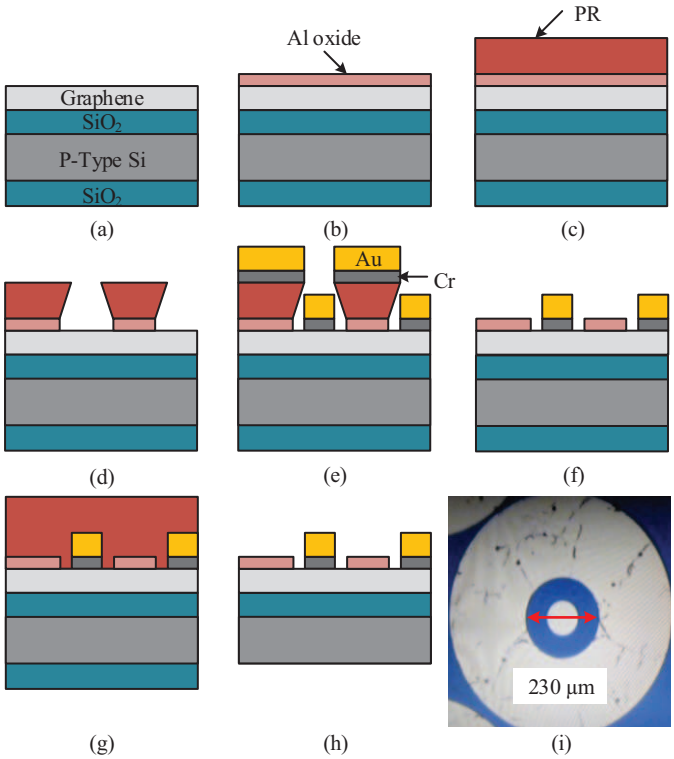

Figure 4.1: (a) RTA cleaned graphene on Si substrate with SiO_2 thermal oxide. (b) Metallization of sacrificial aluminum layer. (c) Spin on photoresist for lithography. (d) Pattern with negative photomask. (e) Metallization of Cr/Au contact layer. (f) Lift-off excess photoresist and metal. (g) Spin on protective photoresist. (h) removal of back SiO_2 oxide with BOE. (i) Photo of finished Corbino disc test structure.

chosen developer not only patterned the photoresist but also selectively etched away the aluminum oxide layer [17]. A 3 nm layer of chromium (Cr) and 30 nm layer of gold (Au) was deposited via e-beam evaporation for electrical contact and a lift-off process was done to finalize the Corbino structure. Cr was chosen as the adhesion layer over Ti in order to more closely match the work function of graphene. The work function

of graphene is approximately $\varphi = 4.56$ eV [26, 27]; that of Au is approximately 5.4 eV whereas those of Ti and Cr are 4.6363 eV and 4.5 eV, respectively. Finally, a protective layer of positive photoresist was spun over the top of the sample and it was immersed in a buffered oxide etchant (BOE) to remove the back layer of SiO_2, a necessary step to allow for contact to the back gate. The Al-oxide passivation layer remains on top of the graphene within the disc structure preventing degradation of the graphene surface when exposed to potential contaminants. This oxide layer could be removed by etching again with the photoresist developer allowing for subsequent processing.

The fabrication step of capping the RTA cleaned sample with a passivation layer is necessary in order to protect the graphene layer during device processing and prevent exposure to ambient air. The Raman spectrum was collected for the processed sample with completed device structures and shows that the graphene is monolayer and remained considerably intact after the fabrication process, Fig. 4.2, [5]. Some defects were created on the graphene during the device processing as shown by the D band peak ($\sim$1350 cm^{-1}) on the Raman spectrum [18].

4.3 DC Characterization

I-V traces of the graphene devices were collected to verify the electrical behavior expected of polycrystalline graphene. Device drain-source (inner disc-outer disc) current versus gate voltage for varying bias voltages was collected using a Keithley 4200 SCS. The data was used to show the point of minimum conductivity, Fig. 4.3,

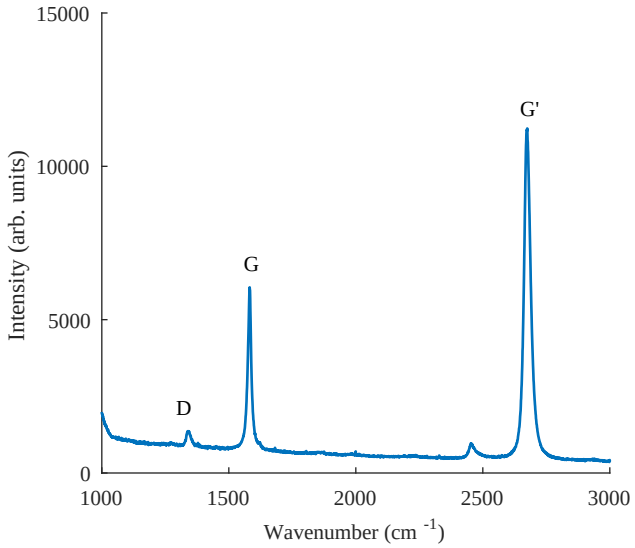

Figure 4.2: Raman spectrum of the processed sample displaying G and G' (2D) peaks as well as a small D peak resulting from disorder in the lattice due to device processing.$I_{G'}/I_G = 1.85$ and $I_G/I_D = 4.43$.

with sheet conductivity (squares per Ohm) given as

$$\sigma_{xx}(\square/\Omega) = \frac{G \ln(r_2/r_1)}{2\pi}, \tag{4.1}$$

where G is the conductance and r_1 and r_2 are the radius of the inner contact and outer contact, respectively [28]. The point of minimum conductivity, the charge neutrality point [29], is displayed between 2 V and 6 V as V_{DS} increases from 1-10 V. The shift in the charge neutrality point of the sample scales with the Drain-Source voltage (V_{DS}), Fig. 4.4. Higher values of V_{DS} create an effective gate voltage that causes the shift. In Fig. 4.5 we have plotted the conductivity, correcting for this effective gate voltage and find that the zero-bias Dirac voltage (V_{Gmin}) lies at 1.5 V.

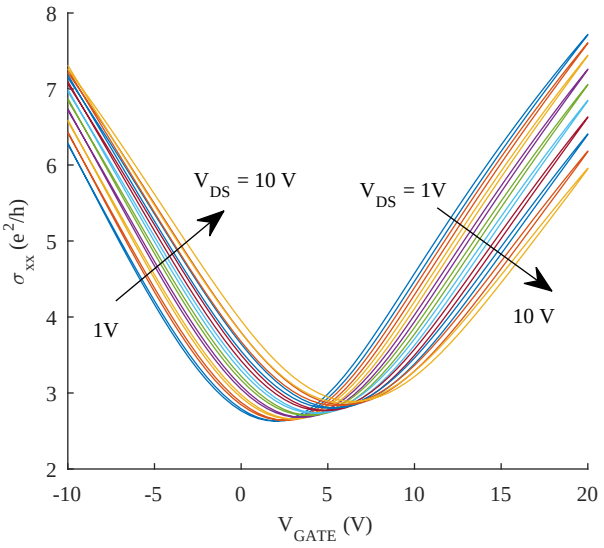

Figure 4.3: Conductivity vs gate voltage for V_{DS} varied between 1 V and 10 V and displaying a charge neutrality point between 2 V and 6 V.

The current-versus-voltage relationship of a traditional semiconductor MOSFET with a Corbino geometry [30] can be modeled in terms of three regimes of operation as

$$\frac{i_D}{k(V_{GS}) \cdot \frac{2\pi}{\ln(r_2/r_1)}} = \begin{cases} 0 & V_{OV} \leq 0 \\ \frac{1}{2}V_{OV}^2(1 + \lambda V_{DS}) & 0 \leq V_{OV} \leq V_{DS} \\ (V_{OV} - \frac{1}{2}V_{DS})V_{DS} & V_{OV} > V_{DS} \end{cases} \tag{4.2}$$

where $k(V_{GS})$ is the product of the carrier mobility (with dependence on the gate-source-voltage difference) and the gate to channel capacitance per unit area, V_{OV} is the overdrive voltage given in terms of a threshold voltage V_t (such that $V_{OV} = V_{GS} - V_t$), and λ is the channel-length modulation effect parameter. Applying these expressions

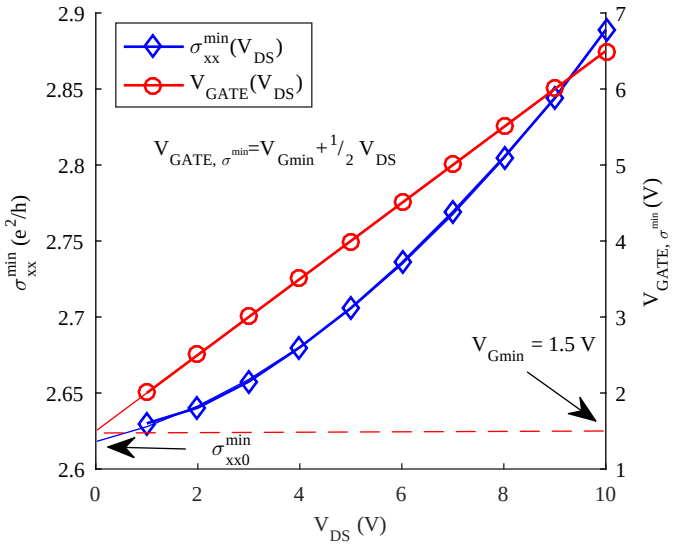

Figure 4.4: Minimum conductivity (left) and it's corresponding gate voltage (right) vs drain-source voltage.

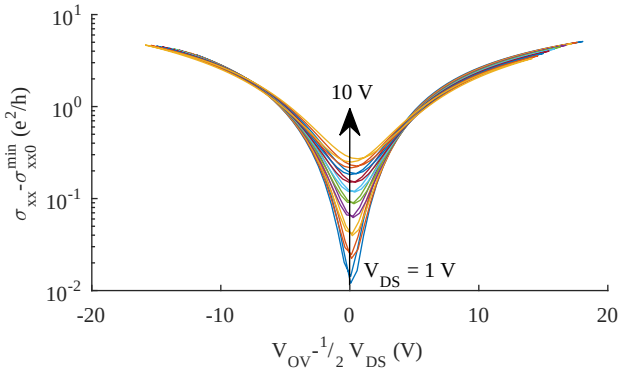

Figure 4.5: Conductivity vs effective gate voltage for V_{DS} varied between 1 V and 10 V, corrected for offset gate voltage.

to Eqn. 4.2, one finds the corresponding large signal conductance to be:

$$\sigma_{xx} = \begin{cases} 0 & V_{OV} \leq 0 \\ \frac{1}{2}k(V_{GS}) \cdot (\lambda + \frac{1}{V_{DS}})V_{OV}^2 & 0 \leq V_{OV} \leq V_{DS} \\ k(V_{GS}) \cdot (V_{OV} - \frac{1}{2}V_{DS}) & V_{OV} > V_{DS}. \end{cases} \tag{4.3}$$

From inspection of Fig. 4.5, we observe that sheet conductance of the channel in our graphene device exhibits behavior of the form

$$\sigma_{xx} = A\sqrt{1 + \left(\frac{\left(V_{OV} - \frac{1}{2}V_{DS}\right)^2}{V_0}\right)} + B, \tag{4.4}$$

with the empirical constants A, V_0 and B. Equation 4.4 can be broken into three regimes of operation analogous to the behavior of the MOSFET:

$$\sigma_{xx} = \begin{cases} \sigma_{xx}^{min} & |V_{OV} - \frac{1}{2}V_{DS}| = 0 \\ C(V_{OV} - \frac{1}{2}V_{DS})^2 + \sigma_{xx}^{min} & 0 \leq |V_{OV} - \frac{1}{2}V_{DS}| \leq V_0 \\ D(V_{OV} - \frac{1}{2}V_{DS}) + E & |V_{OV} - \frac{1}{2}V_{DS}| > V_0, \end{cases} \tag{4.5}$$

where C, D, and E are empirical constants. In this case, the equivalent overdrive voltage is expressed in terms of an experimentally observed gate-voltage offset such that $V_{OV} = V_{GATE} - V_{Gmin}$ and there is an added term σ_{xx}^{min}, which must be due to the minimum conductivity of graphene [31]. Fig. 4.6 shows the three regimes of operation for the case of operation $V_{DS} = 1$ V.

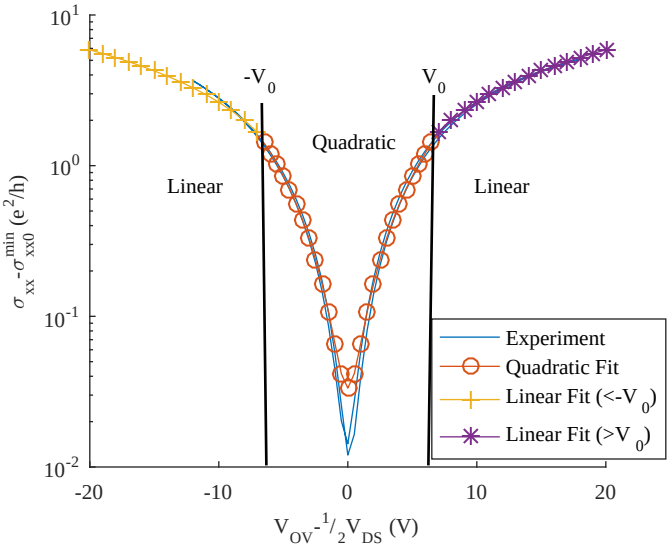

Figure 4.6: Conductivity vs effective gate voltage for $V_{DS} = 1$ V, showing quadratic and linear regions of operation.

4.4 Power Detection

The graphene loaded Corbino disc test structures have been used as microwave power detectors operating at 433.92 MHz. The gated graphene devices were fed with incident microwave power chopped at approximately 1.5 kHz (1501.487 Hz). A voltage measurement was taken via lock-in detection at the chopping frequency on the device under test. An illustration of the experimental structure is shown in Fig. 4.7 and a photograph of the test setup is shown in Fig. 4.8.

Power detection was characterized at both room temperature and liquid nitrogen temperature under vacuum ($<10^{-4}$ Torr) using a Lakeshore Cryotronics CPX-VF probe station with GS-style probes having a ground-to-signal spacing of 250 μm.

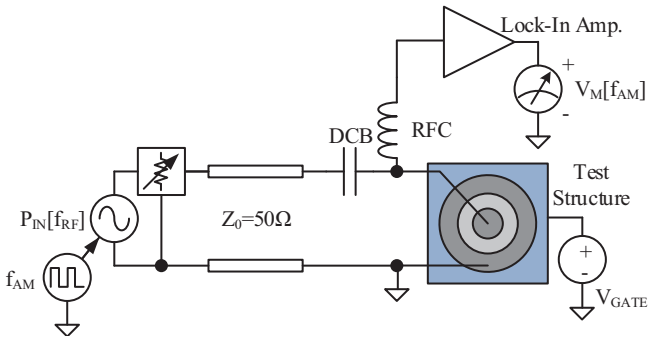

Figure 4.7: Schematic of the graphene power detection circuit.

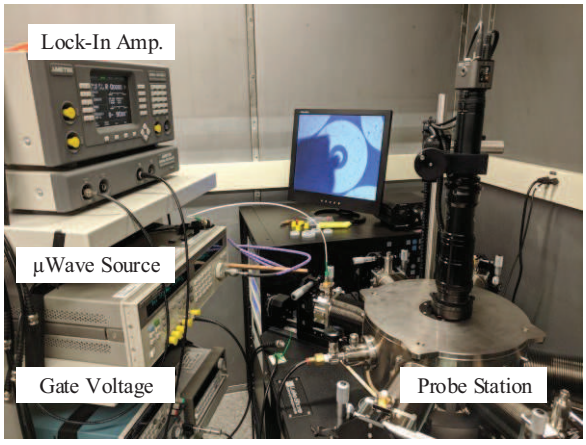

Figure 4.8: Photo of the graphene power detection experimental setup.

Power detection data was collected by sweeping the input power (P_{IN}) and measuring the detected signal (V_M) with the gate voltage (V_{GATE}) chosen to maximize sensitivity as shown in Fig. 4.9. The graphene Corbino disc detectors achieved a peak sensitivity (S_V) of approximately 3.25 mV/mW for a device with an annular area of 40,300 μm^2 at 292 K determined via a fit to the measured data with

$$V_M(\text{dBmV}) = b(\text{dB}) + 2P_{IN}(\text{dBm}), \tag{4.6}$$

where S_V (mV/mW) can be obtained from the log-log plot intercept b (dB) from the relation

$$S_V(\text{mV/mW}) = 10^{\frac{b(\text{dB})}{20\,\text{dB}}}\left(\frac{1\,\text{mW}}{1\,\text{mV}}\right). \tag{4.7}$$

The 1 dB compression point of the detectors occured beyond the range of the available microwave source (>20 dBm at the operating frequency). Power detection measurements done at 80 K improved the sensitivy by approximately 5 dB to peak sensitivity at 5.44 mV/mW for a device with an annular area equal to 38,720 μm^2, Fig. 4.10. The improved graphene detectors exceed the sensitivity of previously reported graphene detectors, 0.86 mV/mW [16], as well as previously explored carbon nanotube bolometers, 0.36 mV/mW, [20, 21]. The detection mechanism of the devices can be attributed to signal rectification due to the nonlinear conductivity of the material.

Measurements were done on devices of varying sizes, with annular areas ranging from 30,200 μm^2 to 40,300 μm^2, and displayed sensitivities from 2.02 μV/mW to 3.25 mV/mW at room temperature. The sensitivity of the devices increases with the annular area of the graphene within the discs. The gate voltage allows for tuning to achieve the maximum sensitivity of the device by altering the gate capacitance and carrier mobility [30] and biasing the material where the conductivity is most nonlinear. The maximum sensitivity was achieved near -17 V at 292 K and shifted down to -12 V at 80 K. The measured voltage response of a 433.92 MHz signal at 0 dBm to a changing gate voltage is shown in Fig. 4.11 for temperatures of both 292 K and 80 K. From inspection of Eqn. 4.5, we see that in the linear regime, the I-V

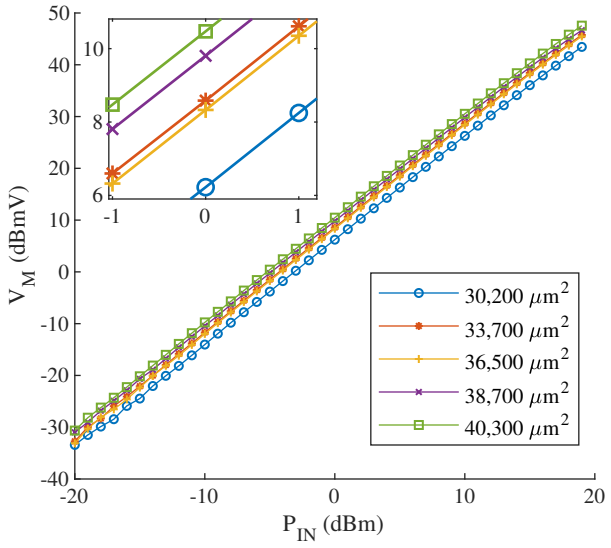

Figure 4.9: Measured voltage vs applied input power at 292 K for multiple disc annular areas (Inset shows zoom-in of plot for clarity).

characteristic can be expanded into the polynomial form of:

$$i_d = g_m V_{DS} + \frac{1}{2} g'_m V_{DS}^2. \tag{4.8}$$

The power detection sensitivity S can therefore be expressed as:

$$|S| = \frac{|g'_m|}{|g_m|} \propto \frac{1}{|V_{OV} + E/D|}. \tag{4.9}$$

This expression indicates that the power detection should fall-off with increasing gate voltage, which is in agreement with our observations shown in Fig. 4.11.

A frequency sweep across the detectors with an incident power of 0 dBm shows the bandwidth of the devices, Fig. 4.12. The detectors can operate up to approximately 1 GHz before there is 3 dB roll-off and power detection falls due to the gate capacitance.

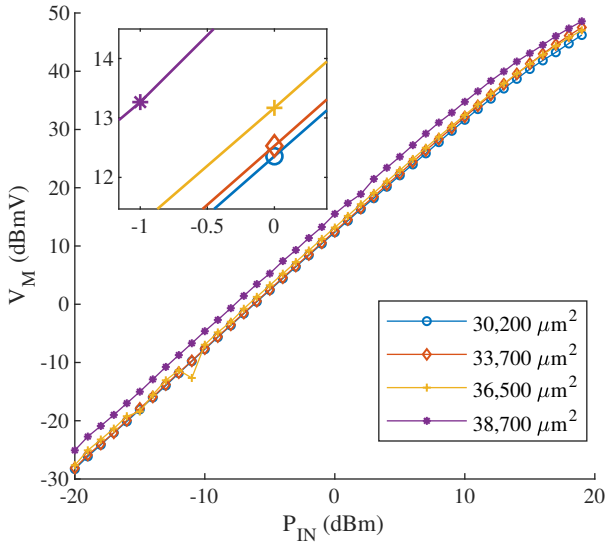

Figure 4.10: Measured voltage vs applied input power at 80 K for multiple disc annular areas (Inset shows zoom-in of plot for clarity).

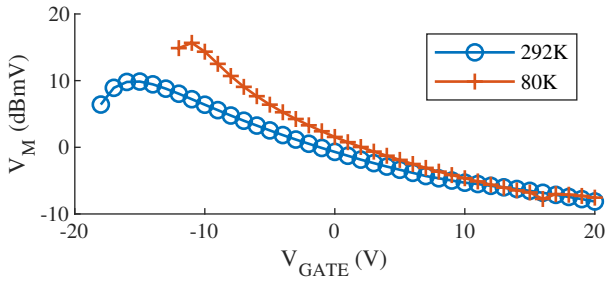

Figure 4.11: Measured voltage vs gate voltage at an incident power of 0 dBm at 433.92 MHz at temperatures of 292 K and 80 K.

4.5 Conclusion

Power detection measurements using graphene Corbino discs yielded a peak power sensitivity of 3.25 mV/mW at room temperature and 5.44 mV/mW at liquid nitrogen

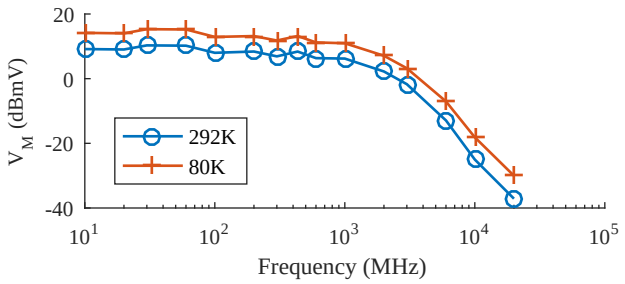

Figure 4.12: Frequency response of a detector showing measured voltage vs frequency at temperatures of 292 K and 80 K.

temperature. We expect that the performance can be improved through continued optimization of the fabrication process and device dimensions. A thicker metal layer will help to increase device yield and prevent damage due to probing. Devices without back gates could help to improve performance at higher frequencies by removing parasitic capacitances, at the loss of tunability via the back-gate voltage.

CHAPTER V

GRAPHENE NANOWIRES

Using commercially-available monolayer graphene, synthesized by means of chemical vapor deposition, microwave power sensing elements have been nanofabricated and integrated with microwave-grade test structures suitable for on-wafer probing. The graphene, situated on a thermal oxide, was first cleaned of stray contaminants in a forming gas environment briefly held at 250 degrees Celsius using a rapid thermal annealer. Immediately following this step, the graphene was passivated with a protective aluminum oxide layer (approximately 5 nm in thickness). Micrometer-scale Corbino disc test structures were then fabricated in direct contact with the graphene using a self-aligned process, which relies on the fact that tetramethylammonium hydroxide develops the photoresist while removing the aluminum oxide. Graphene nanoribbons (with widths as small 400 nm) were then fabricated across the Corbino disc gaps using electron-beam writing in conjunction with a negative tone resist. The same developer exposed the majority of the graphene while defining nanometer-scale lines of photoresist stacked upon aluminum oxide. These stacks served as etch-stops while the unprotected remnants of Al-oxide and graphene were etched in a CF_4/O_2 plasma. Finally, the photoresist was removed leaving behind passivated graphene nanoribbons. Damage caused by the fabrication was evaluated by comparing the Raman spectra of

the graphene before and after microfabrication. Current-versus-voltage traces of the nanodevices exhibited the characteristic conductance minima corresponding to the charge-neutrality point of graphene. Radio frequency power detection experiments at this DC biasing point revealed a detection sensitivity of 0.14 mV/mW. This chapter has been published in the conference paper "Nanoscale Fabrication of Microwave Detectors from Commercially-Available CVD-Grown Monolayer Graphene" presented at the 2018 IEEE Nanotechnology Materials and Devices (NMDC) in Portland, OR on October 14-17, 2018 by Dr. Ryan Toonen [32].

5.1 Introduction

The next generation deep space networks will demand significant improvements in radio frequency (RF) receiver performance. The desire to increase the transmission bandwidth of future deep space explorers while decreasing antenna size creates an opportunity to explore new approaches for realizing ultra-sensitive detectors. The use of graphene in RF detection and mixing applications has received considerable interest due to the unique rectifying characteristics [2] that result from Dirac-cone bandstructure. Additionally, the nanopatterning of graphene into narrow ribbons allows for the opening of an artificial bandgap, which can be engineered by controlling width and crystallographic orientation [33].

This chapter reports on a reliable process for fabricating RF detectors based on graphene nanoribbons (GNRs) that are integrated with Corbino-disc-style microstructures engineered for high-frequency on-wafer probing. The basic structure of

the device is illustrated in Fig. 5.1. The concentric geometry of the probing pad structure is convenient for conducting studies in which both GNR width and crystallographic orientation are varied. Conventional microfabrication techniques were used to produce 100 test structures per 1 cm x 1 cm die with greater than 95% yield. Electron-beam lithography was subsequently used to fabricate GNRs with widths as small as 400 nm. These RF sensing elements were characterized with DC current-versus-voltage measurements to determine the gate-voltage value needed to operate near the conduction minimum associated with the charge-neutrality point of graphene [29]. RF detection experiments with test signals whose frequencies ranged from 10 MHz to 20 GHz were performed using the GNR devices.

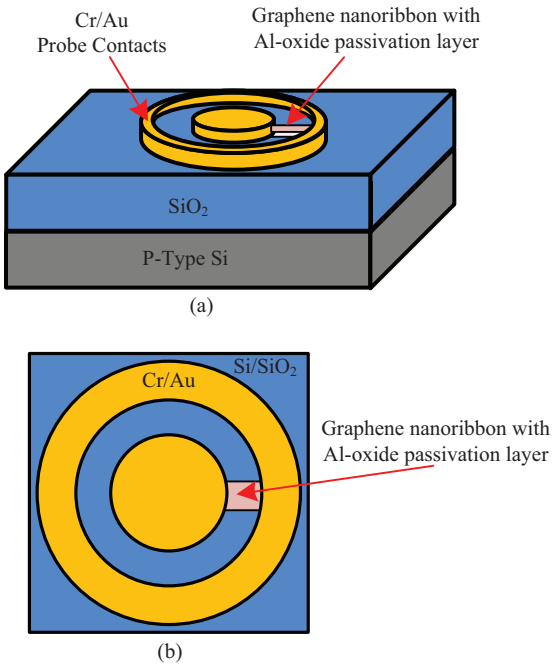

Figure 5.1: GNR loaded Corbino disc profile view (a) and top view (b), not to scale.

5.2 Microfabrication of Corbino Discs

Work has been done in order to improve upon previously reported microfabrication methods [16]. Fig. 5.2 outlines the Corbino disc test structure fabrication process. The process starts by first cleaning commercially available, CVD-grown monolayer graphene on silicon dioxide/silicon (SiO_2/Si), from Graphenea [7], with rapid thermal annealing (RTA) in a forming gas (nitrogen with 4.5% hydrogen) atmosphere at 250 °C for 12 minutes. The RTA helps to reduce impurities absorbed by the graphene surface [7]. Then, a 5 nm sacrificial layer of aluminum (Al) was deposited over the entire substrate and allowed to form a native oxide passivation layer. This complete metallic covering was used to protect the graphene during photolithographic processing. The passivation layer deposition is necessary in order to prevent delamination of the graphene layer during device processing and prevent exposure to ambient contaminants.

A protective layer of positive photoresist, AZ® 4210 by Microchemicals GmbH, was spun over the top of the sample at 500 rpm for 3 seconds followed by 3000 rpm for 42 seconds and hard baked for 30 minutes at 95 °C. The sample was then immersed in a buffered oxide etchant (BOE) for 6 minutes to remove the back layer of SiO_2, to allow for electrical contact to the back gate. Remaining photoresist was removed with acetone, and the Al-oxide passivation layer remained on top of the graphene – preventing degradation of its surface when exposed to potential contaminants.

Adhesion promoter was spun on the sample at 500 rpm for 3 seconds followed by 3000 rpm for 42 seconds and baked on a hotplate at 180 °C for 8 minutes. Image-reversal photoresist, AZ® nLOF 2020 diluted with AZ® Edge Bead Remover (EBR) solvent in a 1:1 ratio [34, 35], was spun on the sample at 500 rpm for 3 seconds followed by 3500 rpm for 42 seconds. The diluted resist spun to a thickness of 400 nm. The edge bead was removed by swabbing the corners of the sample with AZ® EBR, and the samples were soft baked at 110 °C for 15 seconds. The samples were subsequently exposed at an intensity of approximately 15 mW/cm^2 for 1.5 seconds with a subsequent post exposure bake on a hotplate at 110 °C for 3 minutes. The samples were developed in AZ® 300 MIF for 15 seconds. The tetramenthylammonium hydroxide contained in this developer not only contributed to patterning the photoresist but also selectively etched away the Al-oxide layer [17, 36]. A 5 nm layer of chromium (Cr) and 50 nm layer of gold (Au) were deposited via e-beam evaporation for electrical contact. *Lift-off* was performed with MicroChem Remover PG (whose active ingredient is N-methyl-2-pyrrolidone) at 70 °C for approximately 2 hours to finalize the Corbino structure. It is critical to use a stripper that does not attack Al during the lift-off process. The Al-oxide passivation must remain to protect the graphene layer for subsequent nano-processing. Initial implementations of this microfabrication process resulted in a device yield of 95% (95 out of 100 devices were intact) with the majority of device loss being attributed to graphene scratches from substrate handling.

The Raman spectra were collected before and after processing the sample. The spectrum before microfabrication is of the graphene passivated with Al-oxide. Characteristic G and G' peaks are present. Because the Al interferes with the graphene spectrum, a monolayer signature is not obtained at this point in the process. However, the spectrum collected after microfabrication, with passivation removed, showed that the monolayer graphene remained intact, Fig. 5.3, [5]. Some defects were created on the graphene during the device processing as shown by the D band disordered carbon peak ($\sim$1350 cm^{-1}) of the Raman spectrum [18].

5.3 Graphene Nanoribbon Fabrication

Nanometer-scale lines were etched into the graphene between the mircofabricated Corbino disc structures. The same diluted image reversal photoresist used for microfabrication was spun over the Corbino disc structures following the application and soft-baking of AZ® Electronics Grade Adhesion Promoter. Electron beam writing was accomplished using a Hitachi 2460 SEM retrofitted with a fast beam blanker and a Nabity Nanopattern Generation System. The electron beam lithography pattern was aligned to the micro-structures in order to write lines, with widths down to 400 nm, that connected the Corbino disc contacts, Fig. 5.4. The samples were exposed to a dose of 13 μC/cm^2 at a beam current of 20.7 pA with a working distance of approximately 11 mm. After electron beam writing the sample was developed in AZ® 300 MIF for 15 seconds. The patterned photoresist served as an etch-stop while the unprotected graphene and remnants of Al-oxide were dry-etched in a reactive ion

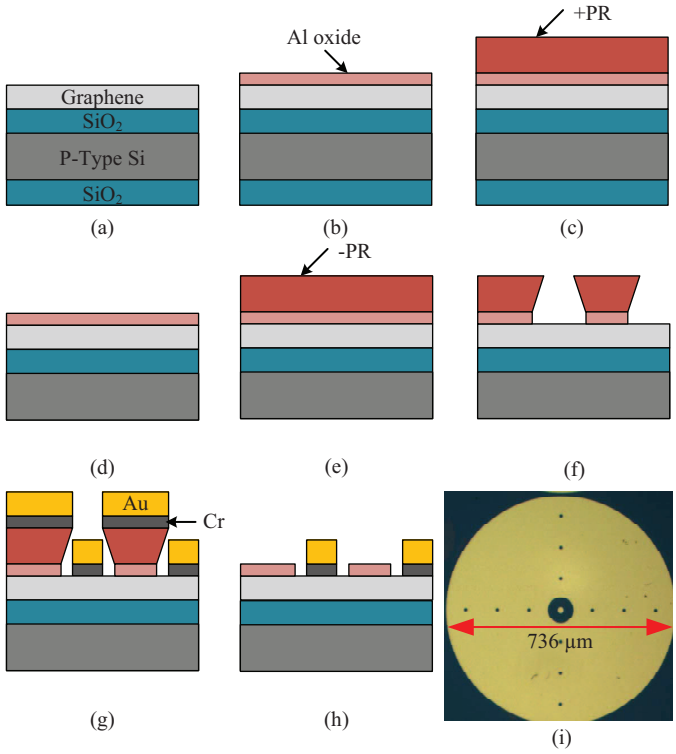

Figure 5.2: (a) RTA cleaned graphene on Si substrate with SiO_2 thermal oxide. (b) Metallization of sacrificial Al layer. (c) Spin on positive photoresist for BOE. (d) removal of back SiO_2 oxide with BOE. (e) Spin on negative photoresist for microlithography. (f) Pattern with negative photomask. (g) Metallization of Cr/Au contact layer. (h) Lift-off excess photoresist and metal. (i) Photograph of finished Corbino disc test structure.

etcher (RIE). The RIE was done for 15 seconds in a gaseous composition of 80% CF_4 and 20% O_2 with a flow rate of 15 sccm [37]. The power was set to 150 W, and the pressure was maintained at 170 mTorr. Finally, the photoresist was removed, with MicroChem Remover PG, leaving behind passivated GNRs. The sensitive to precise

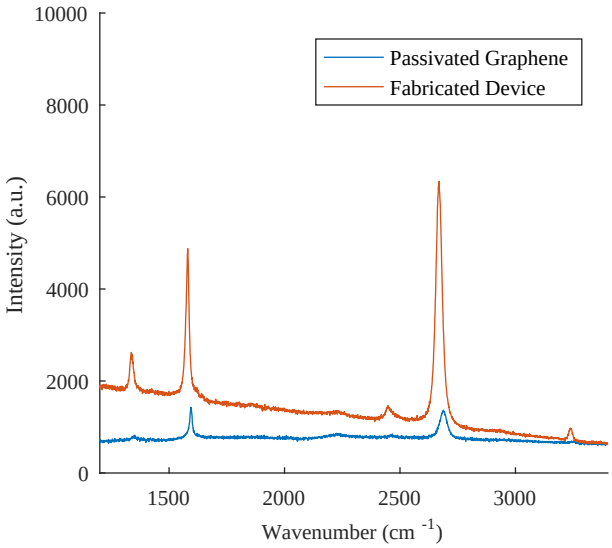

Figure 5.3: Raman spectra of the passivated sample before device processing and spectrum of the sample after the microfabrication process.

timing during the development and etching steps reduced device yield to 83%. Fig. 5.5 shows a photograph of a completed device.

5.4 Electrical Characterization of Graphene

DC current versus voltage traces were collected to verify continuity of the nanowire between the contacts of the Corbino disc electrodes. Device drain-source (inner disc-outer disc) current versus gate voltage for varying bias voltages was collected using a Keithley 4200 Semiconductor Characterization System, Fig 5.6. The data shows that the charge neutrality point occurred near 30 V. The large shift away from the

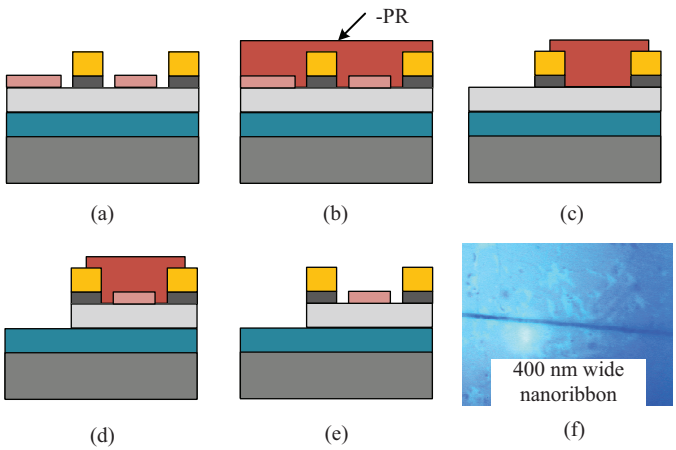

Figure 5.4: (a) Graphene Corbino discs from microfabrication process. (b) Spin-on image-reversal photoresist for electron beam writing. (c) Nanoribbon photoresist patterns in Corbino disc gap. (d) Ion-milling of exposed graphene. (e) Stripping of remaining photoresist. (f) Photograph of GNR with Al-oxide passivation. The contrast has been altered for clarity.

expected value of 0 V is likely due to residual contaminants from material processing.

The GNRs have been used to realize microwave power detectors operating from 10 MHz to 20 GHz. The devices were biased with $V_G = 30$ V as determined from the DC current-voltage traces. The devices were fed with incident microwave power chopped at 1.5 kHz. A voltage measurement was taken via lock-in detection at the chopping frequency that modulated the microwave power. A schematic of the apparatus is shown in Fig. 5.7. Fig 5.8 shows the frequency dependence of power detection sensitivity with incident microwave power set to a constant value of

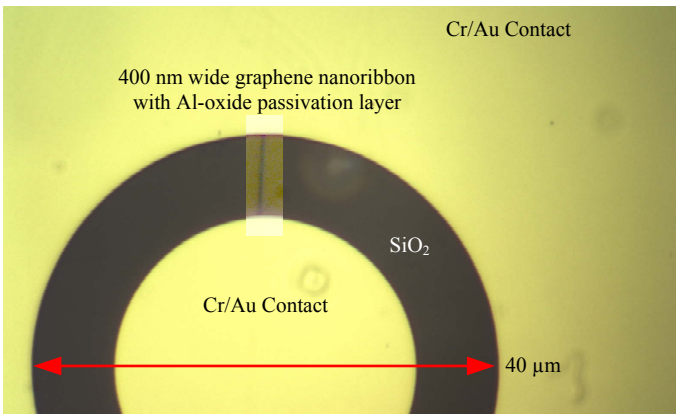

Figure 5.5: Microscope photograph of a GNR integrated into a microfabricated Corbino disc test structure. The contrast of the area around the GNR has been adjusted for clarity.

0 dBm. Fig 5.9 shows a power sweep from -20 dBm to 15 dBm with the microwave signal frequency set to 2.4 GHz. The detector shows a power sensitivity of 0.14 mV/mW. Previously explored graphene detectors have shown sensitivities of up to 5.43 mV/mW [16]. However, the data presented in this paper does not take into consideration the GNR power detection efficiency. The relatively large impedance of the device is expected to cause significant reflection of power; so, impedance matching would increase the power detection sensitivity. Power detection is due to rectification resulting from the Dirac cone band structure. From inspection of Fig. 6.3, it can be seen that the I-V characteristic can be expanded into the polynomial form of:

$$i_d = g_m V_{DS} + \frac{1}{2} g'_m V_{DS}^2 \tag{5.1}$$

where the second order term gives rise to rectification.

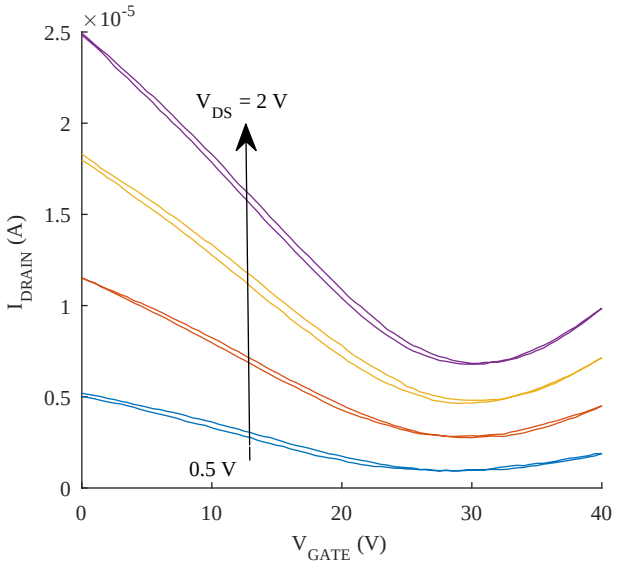

Figure 5.6: Drain-source current versus gate voltage for V_{DS} varied between 0.5 V and 2 V. The point of minimum conductivity is near 30 V.

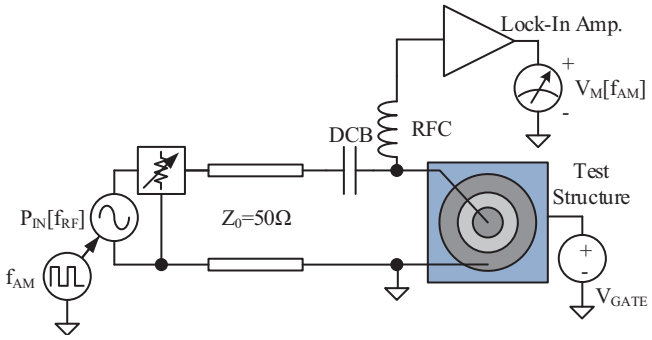

Figure 5.7: Schematic of the graphene power detection circuit.

5.5 Conclusions

Our simple one mask microfabrication process has a device yield of 95%. However, final steps in the nanofabrication process reduce this high yield. The final develop-

ment etches the remaining Al-oxide but can also undercut the nano-patterned lines and remove the structures. The ion-milling step may also result in damaged devices. Work must be done to optimize these two final process steps. The developer may be diluted to offer more latitude in the timing before undercutting the oxide and removing structures. The timing and gas composition of the reactive ion etch may also be optimized to better attack the Al-oxide while leaving the photoresist layer intact.

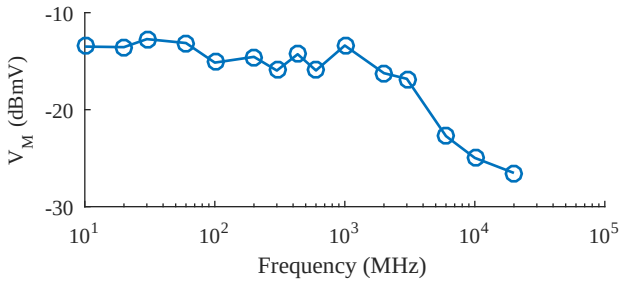

Figure 5.8: Frequency response of GNR detector.

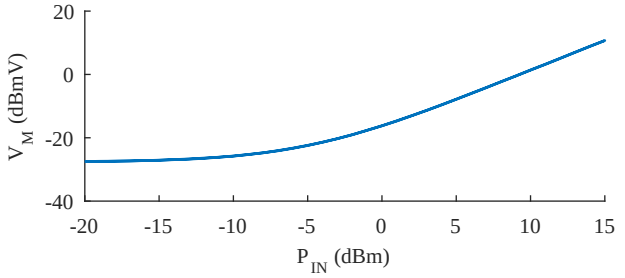

Figure 5.9: Measured voltage vs applied input power at room temperature of a GNR detector.

CHAPTER VI

GRAPHENE NANOCONSTRICTIONS

Microwave power detectors were realized using nano-constrictions fabricated from commercially-available monolayer graphene, synthesized by means of chemical vapor deposition. The graphene nano-constrictions (GNCs) were fabricated so as to shunt the inner discs to the concentric outer annuli of micrometer-scale Corbino disc test structures. The test structure was fabricated on a layer of electrically-insulating silicon dioxide situated on an electrically-conductive, doped silicon substrate. The substrate was used as a gate for controlling the Fermi level in the nano-constriction. Probe station measurements were conducted on a detector with nano-constriction dimensions of 500 nanometers in width and 5 micrometers in length. The annulus of this device was electrically grounded and held in thermal equilibrium with chassis of the probe station. Measurements obtained with a vector network analyzer provided the reflection coefficient of the detector. Using a test signal frequency of 433.92 MHz, microwave power detection characterizations, which accounted for signal reflection, revealed a peak detection sensitivity of 60.25 mV/mW. The gate voltage dependence of the power detection sensitivity was found to be strongly correlated with that of the Mott formula used for calculating the Seebeck coefficient of graphene. This observation suggests that localized microwave heating of the inner disc, relative

to the temperature of the outer annulus, establishes a thermal gradient across the nano-constriction and results in a thermoelectric response that is proportional to the power level of the incident microwave signal. This chapter is the basis of the journal paper "Thermoelectric Graphene Nano-Constrictions as Detectors of Microwave Signals" published in IEEE TRANSACTIONS ON NANOTECHNOLOGY [38].

6.1 Introduction

The next generation deep space networks will demand significant improvements in radio frequency (RF) receiver performance. The desire to increase the transmission bandwidth of future deep space explorers while decreasing antenna size creates an opportunity to explore new approaches for realizing ultra-sensitive detectors. The use of graphene in RF detection and mixing applications has received considerable interest due to the unique rectifying characteristics [2] that result from Dirac-cone bandstructure. Additionally, the nanopatterning of graphene into narrow ribbons allows for the opening of an artificial bandgap, which can be engineered by controlling width and crystallographic orientation [33]. Graphene has also been used in photodetection schemes as well as an absorbing material in optically transparent antennas and detectors [3, 39, 40, 41]. While photodetection at microwave frequencies has been shown at cryogenic temperatures with suspended ultraclean graphene [42], we have demonstrated room-temperature microwave detection using on-wafer graphene processed using standard techniques.

In this paper, we report on improved device processing and performance over those previously explored in [32]. Microwave detectors based on graphene nanoconstrictions (GNCs) are integrated with Corbino-disc-style microstructures engineered for high-frequency on-wafer probing. The concentric geometry of the probing pad structure is convenient for conducting studies in which both GNC width and crystallographic orientation are varied. Conventional microfabrication techniques were used to produce 100 test structures per 1 cm x 1 cm die with greater than 95% yield. Electron-beam lithography was subsequently used to fabricate GNCs. These microwave sensing elements were characterized with DC conductance vs gate voltage measurements to determine the Fermi level dependence of the Seebeck coefficient [29]. These GNC detectors were used to detect continuous-wave signals with frequencies ranging from 10 MHz to 10 GHz. The Fermi-level dependence of the microwave power detection sensitivity was strongly correlated with that of the Seebeck coefficient suggesting that the dominant physical mechanism of detection is the thermoelectric effect. Network analyzer measurements were collected in order to determine the amount of unreflected power that was delivered to the detector. The sensitivity of the devices has been determined with respect to the unreflected power, resulting in significantly higher values than previously reported [32]. In comparison to thermoelectric detectors based on CMOS and MEMS technologies [43, 44, 45, 46]-which offer relatively low power detection sensitivity but are widely used in applications requiring high linearity and zero DC power consumption [47]-our graphene detectors exhibit a significant improvement in power detection sensitivity (up to one order of

magnitude). The improvement is three orders of magnitude greater when accounting for signal reflection due to impedance mismatch.

6.2 Fabrication of Corbino Discs and Graphene Nano Devices

With respect to previous work reported by the authors, an improved micro-fabrication process was developed [32]. Fig. 6.1 outlines the improved method for fabricating Corbino disc test structures. The process begins by cleaning commercially-available, CVD-grown, monolayer graphene that has been previously transferred to a 300-nm thick silicon dioxide layer that was thermally grown on a p-type silicon substrate [7], with rapid thermal annealing (RTA) in a forming gas (nitrogen with 4.5% hydrogen) atmosphere at 250 °C for 12 minutes. The RTA is a critical step to reduce impurities on the graphene surface [7, 48]. A 5 nm sacrificial layer of aluminum (Al) was deposited over the entire substrate and allowed to form a native oxide passivation layer [17]. This complete metallic covering was used to protect the graphene during photolithographic processing. The passivation layer deposition is necessary in order to prevent delamination of the graphene layer during device processing and prevent exposure to ambient contaminants. The back layer of SiO_2 is removed using the same process described in [32].

The graphene is then patched in order to isolate individual devices and allow for better adhesion of metal contacts. Positive tone photoresist, AZ®5214-E was spun on the sample at 500 rpm for 3 seconds followed by 4000 rpm for 42 seconds. The edge bead was removed by swabbing the corners of the sample with AZ® EBR, and

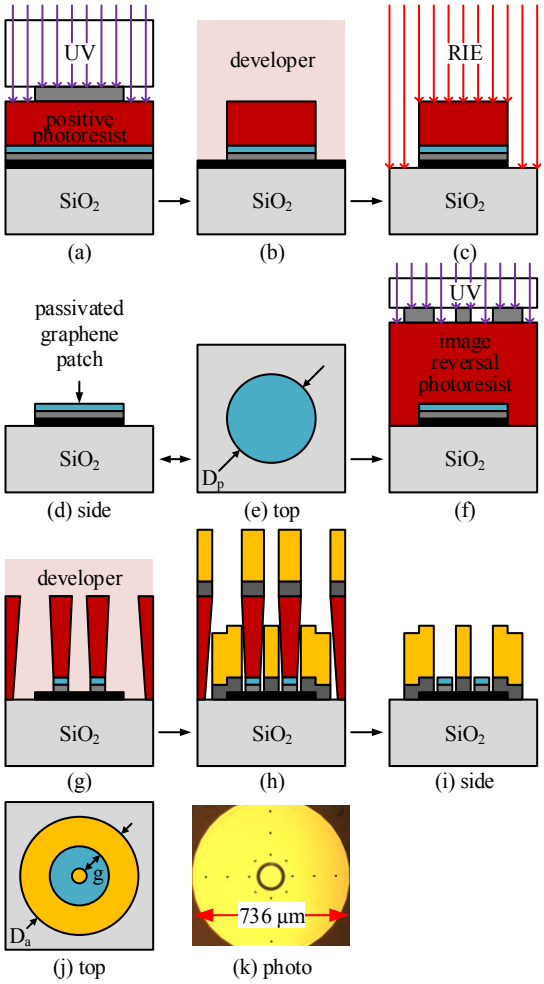

Figure 6.1: Photolithography to patch the graphene/Al stack (a). Development and etching for patching (b) and (c). Remaing graphene patches (d) and (e). Standard photolithographic processing of Cr/Au Corbino discs (f)-(j). Microscope photograph of Corbino disc test structure after micro-fabrication (k).

the samples were soft baked at 110 °C for 3 minutes. The samples were subsequently exposed at an intensity of approximately 15 mW/cm^2 for 20 seconds, Fig. 6.1 (a), followed by a development in AZ® 300 MIF for 30 seconds. The developer contains

tetramethylammonium hydroxide which selectively etches areas of exposed Al/Al oxide, leaving only bare graphene Fig. 6.1 (b). The remaining resist acted as an etch stop [36] as the samples were placed in an reactive ion etch of O_2/Ar for 60 seconds at 100 W, Fig. 6.1 (c). The resist, which was left behind after the RIE treatment, was removed with acetone. Passivated graphene patches remained on the substrate, Fig. 6.1 (d) and (e). The patterning of the Cr/Au contacts follows the same procedure outlined in [32].

Dogbone shapes with nano-constrictions were etched from the passivated graphene situated between the inner disc and outer annuli of the Corbino disc test structures. Negative tone E-Beam resist Dow Corning XR-1541-006 (HSQ) was used for the process. The diluted resist previously used for E-Beam lithography was exposed too quickly, with a low dose to print, and had poor resolution as a result. E-beam writing was accomplished using a Hitachi 2460 SEM retrofitted with a fast beam blanker and a Nabity Nanopattern Generation System. The electron beam lithography pattern was aligned to the micro-structures in order to write lines that connected the Corbino disc contacts, Fig. 6.2. The samples were exposed with a dose of 400 μC/cm^2 at a beam current of 10 pA at 30 kV with a working distance of approximately 12 mm, Fig. 6.2 (a).

After electron beam writing the sample was developed in AZ® 300 MIF for 4 minutes. The e-beam resist that remained on top of the graphene/Al stack hardened into glass, Fig. 6.2 (b). However, the hardened resist acts as another layer of passivation to protect the device. The patterned photoresist served as an etch-stop

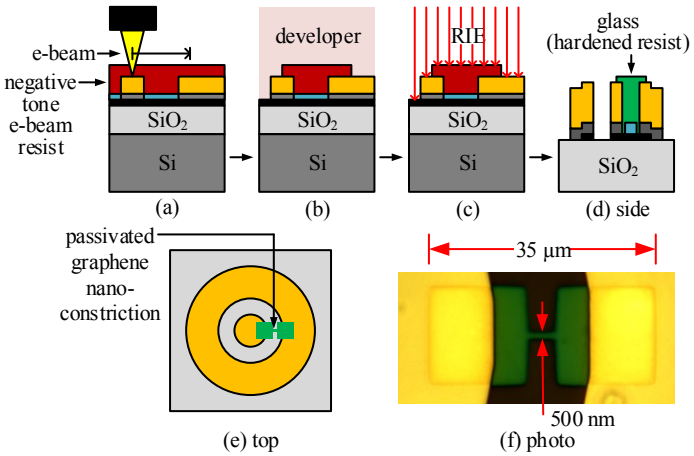

Figure 6.2: Fabrication of GNCs using electron-beam writing (a), development leaving behind the hardened resist (b), and etching excess graphene (c). Final device structure is shown in (d) and (e) with microscope photograph of nano-constriction in a *dogbone* configuration (f). Illustrations are not to scale.

while the unprotected graphene and remnants of Al-oxide were dry-etched in an RIE, Fig. 6.2 (c). The RIE was done in O_2/Ar for 2 minutes at 150 W. Future devices should use a smaller amount of aluminum passivation, the Al-oxide layer hardens during processing and can prove difficult to remove. Fig. 6.2 (f) shows a photograph of a completed device.

6.3 Electrical Characterization of GNCs

DC current versus voltage traces were collected to verify continuity of the GNC as well as locate minimum conductivity point of the graphene. Device conductance drain-source (inner disc-outer disc) current versus gate voltage for varying bias voltages was

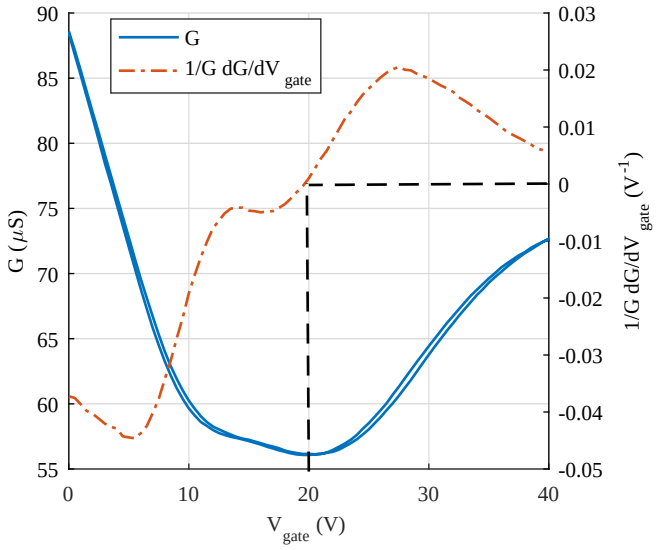

Figure 6.3: Drain-Source conductance as a function of Gate voltage with Drain-Source voltage held at 100 mV (left) and derivative of conductance scaled by resistance (right). Device displays a conductance minimum at 20 V.

collected using a Keithley 4200 Semiconductor Characterization System. The device conductance

$$G = \frac{I_{DS}}{V_{DS}} \tag{6.1}$$

is plotted in Fig 6.3 along with its derivative. The data verifies the ambipolar curve characteristic of graphene with the charge neutrality point at 20 V, improved over the 30 V point shown in our previous GNC devices. We attribute the improvement to refinements made in device processing.

The GNCs have been used to realize microwave power detectors operating from 10 MHz to 10 GHz at room temperature and under vacuum. To determine the

fraction of incident that was not reflected off of the detector, reflection coefficient Γ measurements were collected with an Agilent E5071C vector network analyzer. Prior to these collecting these measurements, a reference plane was defined at the probe tips by means of a short-open-load calibration using a GGB Industries, Inc. CS-8 calibration substrate, Fig. 6.4. Monolayer graphene on SiO_2 is very sensitive to scattering and shows reflection very close to that of an open circuit [49]. At our operating frequency of 433.92 MHz the reflection coefficient was -0.185 dB. The power P_L delivered to the detector (an effective load) is related to the power P_S from the signal generator by

$$P_L = P_S(1 - |\Gamma|^2). \tag{6.2}$$

The operating frequency of 433.92 MHz was chosen for being in the middle of an unlicensed ISM band as well as being within the frequency range before there is detection roll-off for the GNC device. A frequency sweep from 10 MHz to 10 GHz done with a constant power at the load of -12.9 dBm and gate voltage of 0 V displays -3 dB roll-off on detection at 1 GHz, Fig 6.4. The devices were then probed with incident microwave power through a bias tee, consisting of a DC Block (DCB) and RF choke (RFC), and a resulting voltage was measured directly with a digital voltmeter. A schematic of the experimental setup is shown in Fig. 6.5. The gate voltage was stepped from 0 V to 40 V to capture the area around the charge neutrality point and the power at the load was swept from -54 dBm to -4 dBm. The results of the detection measurement are shown in Fig. 6.6.

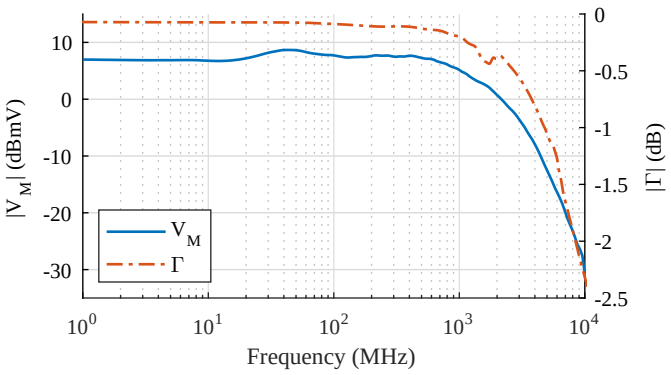

Figure 6.4: Frequency response of GNC detector with $P_L = -12.9$ dBm and $V_{gate} = 0$ V (left) and reflection coefficient of GNC structure (right). Reflections decrease as frequency increases due to the capacitive design of the Corbino disc microstructure.

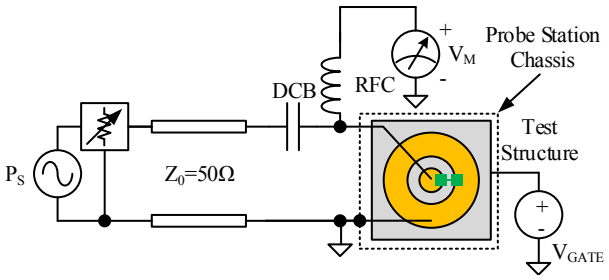

Figure 6.5: Schematic of experimental setup. The GNC device was probed with a Lakeshore Cryotronics CPX-VF probe station at ambient temperature, approximately 20 °C (293 K), and vacuum pressure of 8.7×10^{-7} Torr.

Observing the measured voltage as a function of gate voltage, Fig. 6.7, we can see a minimum appear at the Dirac voltage. This minimum represents a change in polarity of the measured voltage. Plotting this data linearly, Fig. 6.8, shows that

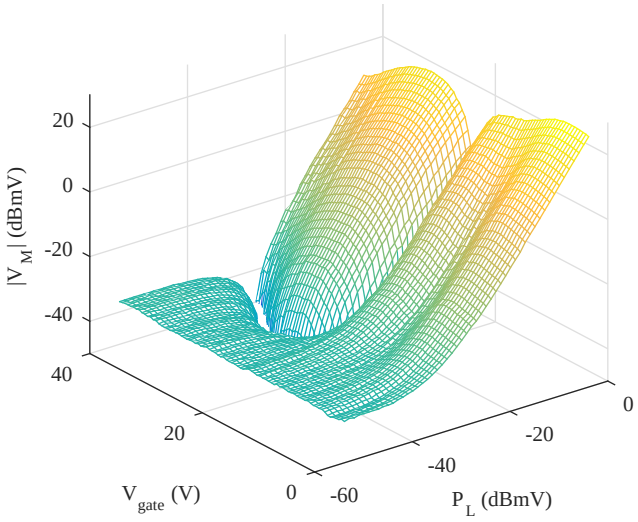

Figure 6.6: Raw data of measured voltage as a function of both the gate voltage and the power delivered to the detector.

it is proportional to the Seebeck coefficient

$$V_M \propto \frac{1}{G}\frac{dG}{dV_{gate}} \propto S \tag{6.3}$$

where the Seebeck coefficient S is given by the Mott formula,

$$S = -\frac{\pi^2 k_B^2 T}{3|e|}\frac{1}{G}\frac{dG}{dV_{gate}}\frac{dV_{gate}}{dE}\bigg|_{E=E_F}, \tag{6.4}$$

matching the behavior previously observed from graphene-based photothermoelectric detectors [50, 1, 3]. The change in polarity of the measured voltage occurs at the charge neutrality point. The sensitivity of the detector is extracted by fitting the linearly scaled V_M and P_L to

$$V_M^2 = V_N^2 + (S_V P_L)^2. \tag{6.5}$$

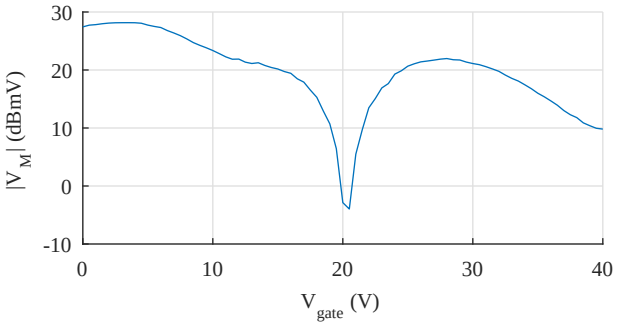

Figure 6.7: Raw data of measured voltage versus gate voltage with an applied power of 10 dBm, top, a cross section of Fig. 6.6. The minimum shown at $V_{GATE} = 20$ V represents a change in the polarity of V_M.

The maximum sensitivity was obtained for a gate bias voltage of approximately $V_{gate} = 1$ V and was found to be $S_V = 60.25$ mV/mW, Fig. 6.9. When not accounting for impedance mismatch, the uncompensated power detection sensitivity (relative to P_S rather than P_L) is 2.394 mV/mW.

Strong correlation between the gate-voltage dependence of the DC measurement of $\frac{1}{G}\frac{dG}{dV_{gate}}$ and voltage response to incident microwave power indicates that the thermoelectric effect is the dominant physical mechanism responsible for microwave power detection. Incident microwave power locally heats the inner disc (the drain node) of the Corbino disc test structure while the outer annulus (the source node) is held in thermal contact with probe station chassis. Thus, a temperature gradient develops across the nano-constriction and charge carriers diffuse towards the detector's source node, the cooler side of the constriction. When the gate voltage is biased below the 20 V charge-neutrality point, the Fermi level is situated below the valence band

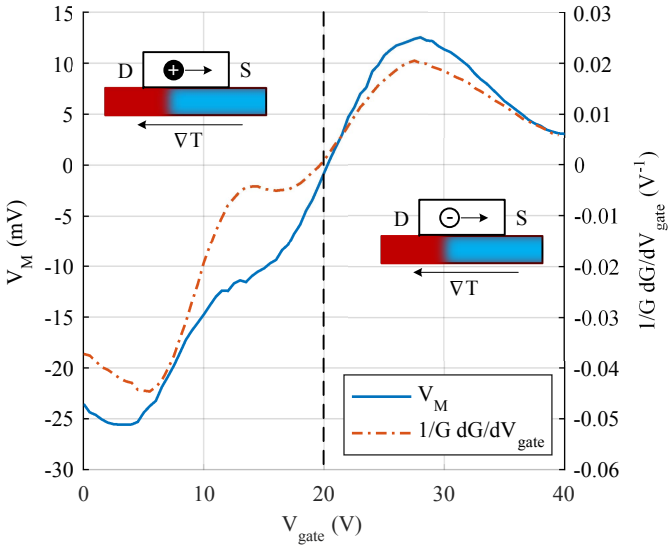

Figure 6.8: Measured voltage versus gate voltage with an applied power of 10 dBm, scaled linearly, showing the sign change in measured voltage due to a change in majority carriers caused by varying the gate voltage. It can be seen that the measured voltage is proportional to the Seebek Coefficient, $V_M \propto S$.

edge of the Dirac cone and positively-charged holes are the majority charge carrier in the graphene. With an accumulation of positive charge on the source-node side of the GNC, a negative voltage develops across the detector. Conversely, when the gate voltage is biased above the charge-neutrality point, negatively-charged electrons are the majority carrier in the graphene, and a negative voltage develops across the detector.

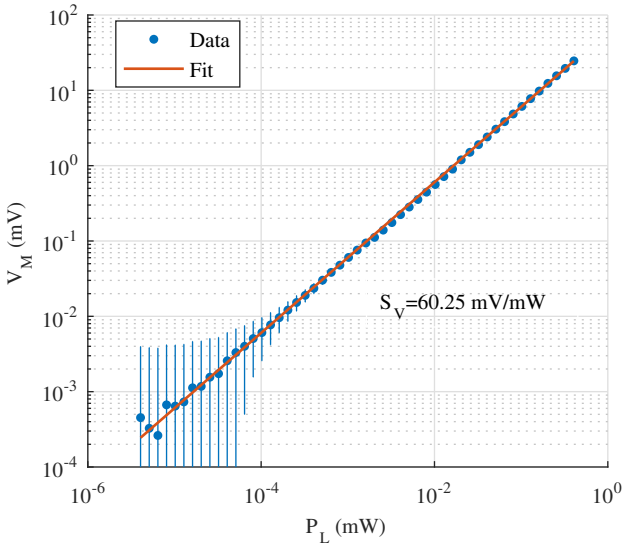

Figure 6.9: Measured voltage versus power delivered to the detector with $V_{gate} = 1$ V.

6.4 Cryogenic Device Measurements

The measurements for GNC DC characterization and microwave power detection were repeated at a temperature of 80 K on a device with a constriction width of 100 nm. The results of the DC measurements are shown in Fig. 6.10 and the results of the power detection measurements are shown in Fig. 6.11. The data once again shows correlation, although not as strong, between the gate-voltage dependence of the DC measurement of $\frac{1}{G}\frac{dG}{dV_{gate}}$ and voltage response to incident microwave powe that had been seen with the larger, room temperature device. A width of 100 nm approaches the resolution limit of the equipment used to fabricate the devices. Oscillations can

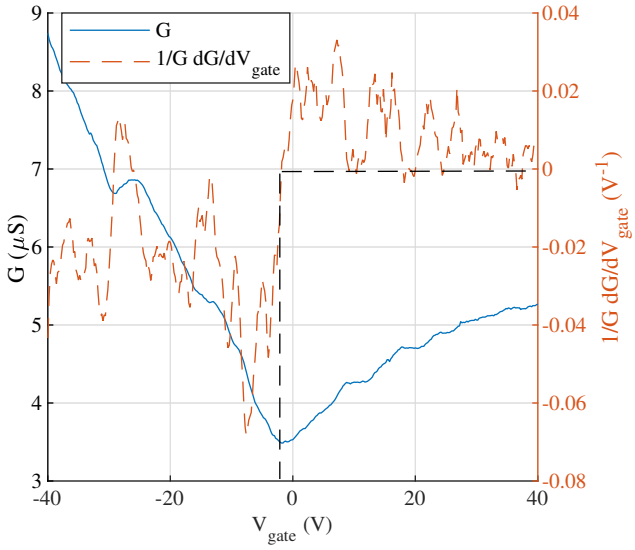

Figure 6.10: Drain-Source conductance as a function of Gate voltage with Drain-Source voltage held at 100 mV (left) and derivative of conductance scaled by resistance (right). Device displays a conductance minimum at -1.8 V.

be seen in the voltage response to incident microwave power which correspond to plateaus observed in the DC conductivity.

6.5 Conclusions

Microwave power detectors based on GNCs have been demonstrated at room temperature. Experiments indicate that the thermoelectric effect is the dominant detection mechanism. The thermoelectric effect in graphene has been previously used to enable power detection of signals with operating frequencies of 300 GHz [1] as well 582.7

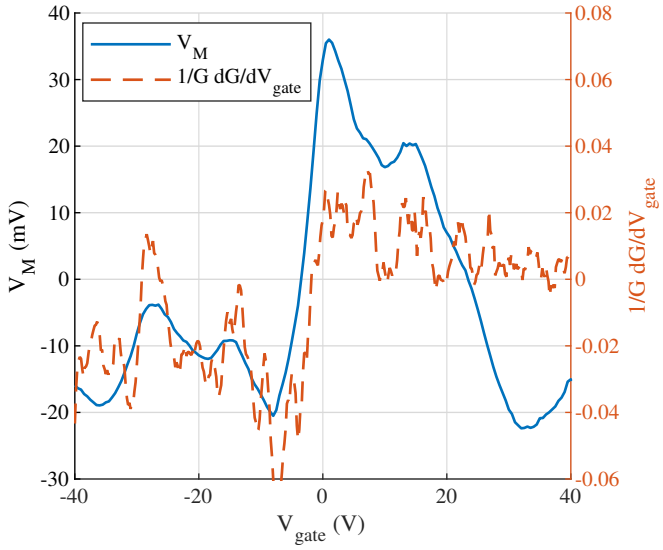

Figure 6.11: Measured votlage versus gate voltage with an applied power of 10 dBm, rescaled linearly, showing the sign change in measured voltage due to change in majority carriers caused by varying the gate voltage.

THz (514.5 nm) [51]. Our demonstration at 433.92 MHz suggests the possibility of enabling multi-spectral sensing with a single integrated device technology.

When accounting for signal reflection due to impedance mismatch, our detector yielded an effective power detection sensitivity of 60.25 mV/mW. Commercially-available detectors that feature zero DC power consumption and operate over similar frequency ranges typically offer a power detection sensitivity of 500 mV/mW [52]. However, state-of-the-art thermoelectric detectors based on CMOS and MEMS technologies [43, 44, 45, 46, 47] offer power detection sensitivities that are typically lower than 0.4 mV/mW. Without compensating for signal reflection, our thermoelectric de-

tector yielded a power detection sensitivity of 2.394 mV/mW, which by comparison is also a significant improvement. We expect that optimization of the GNC and Corbino disc dimensions as well as reduction of the parasitic capacitance resulting from the back-gate will lead to improvements in sensitivity as well as frequency response.

CHAPTER VII

GRAPHENE LOADED RESONATOR DESIGN

Prior work discussed in Ch.6 has shown that power has not been efficiently delivered to the graphene nano-constrictions (GNRs). A new structure for contacting the graphene was designed for more efficient power detection. A coplanar waveguide half-wave resonator was used to more efficiently deliver power to the graphene nano-constriction. The GNRs have shown typical resistances ranging from 10-100 kΩ (comparable to the Klitzing constant, ∼25.8 kΩ). A resonator structure was chosen to address the difficulty of matching this high impedance with the characteristic 50 Ω impedance typical of microwave structures. These half-wave resonators were simulated and constructed on a sapphire substrate in order to reduce the size of the required structure. The waveguide contained an integrated gate for controlling the Fermi level in the nano-constriction. Probe station measurements were conducted using a vector network analyzer to determine the resonant frequency of the device.

7.1 Coplanar Waveguide Specification

The graphene load is designed to be placed at the anti-nodes of the half wave resonator. The large impedance of the graphene should act as a small perturbation and not hamper the performance of the resonator. Fig. 7.1 shows a simple diagram of the

proposed structure where the graphene is placed at the point of maximum electric field.

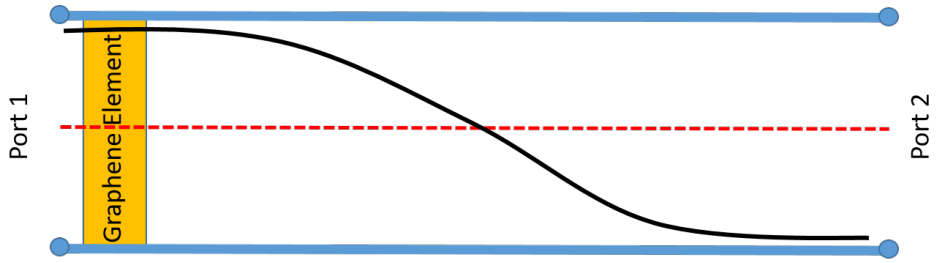

Figure 7.1: Cartoon of half-wave resonator showing graphene at the anti-node.

The structures are specified to operate at 62 GHz, moving towards. A sapphire substrate is chosen and it has a relative permittivity of $\epsilon_r = 10$, the substrate thickeness used is 432 μm. With this thickness and relative permittivity, along with constraints on probe spacing, dimension of $W = 100$ μm and $S = 50$ μm are chosen. This gives a characteristic impedance of approximately 51.6 Ω and an effective permittivity of $\epsilon_r = 5.458$. At 62 GHz the guided wavelength is $\lambda_g = 2.071$ mm.

7.1.1 Material Processing

The thickness of the waveguide metal layer needed to meet skin depth requirements cannot be achieved with the previously described lithographic processing methods. The photoresist thickness when spun on the substrates is too thin compared to the required metal thickness. Attempts at using the nLOF2020 and spinning it a slower speed for a thicker layer of resist have been unsuccessful. The thickness of the nLOF2020 at low speeds is not uniform and results in poor mask contact/exposure

during photolithography. A thicker photoresist, Z® nLOF 2070, was used in order to realize the thick metal structures.

The samples were first spun the adhesion promoter at 500 rpm for 3 seconds followed by 3000 rpm for 55 seconds and baked on a hot-plate 180 °C for 8 minutes. Image-reversal photoresist, AZ® nLOF 2070 was then spun on the sample at 500 rpm for 3 seconds followed by 7000 rpm for 55 seconds. The resist spun to a thickness of 8 μm. The edge bead was removed by swabbing the corners of the sample with AZ® EBR. The samples were soft baked at 110 °C for 90 seconds. The samples were immediately exposed after baking at an intensity of approximately 15 mW/cm^2 for 3.5 seconds with a subsequent post exposure bake on a hotplate at 110 °C for 60 seconds. The samples were developed in AZ® 300 MIF for 30 seconds and rinsed with deionized water, the development step was then repeated once. A 50 nm layer of titanium (Ti) and 3 μm layer of gold (Au) were deposited via e-beam evaporation for electrical contact.

Nanoprocessing of the material also requires a new method. Electron beam lithography requires a conducting substrate to achieve fine resolutions. A nonconductive substrate, such as sapphire, causes charge to build up and perturb the electron beam during writing. Fine lines and gaps can not be resolved due to this effect. A spin on conductive polymer was used to mitigate this proximity effect and charge buildup. Spinning a conductive polymer on top of the HSQ resist will dissipate the charge during E-beam writing and allow fine lines and gaps to be resolved. The nanolithographic process remains mostly the same as previously described for HSQ,

the exception being that after baking the HSQ samples were spun with PEDOT:PSS conductive polymer at 500 rpm for 3 seconds followed by 5000 rpm for 55 seconds. After exposure and before development the PEDOT:PSS was removed in a bath of DI water for 60 seconds.

7.2 Results

Two types of resonators were simulated and constructed for testing. A resonator with a single graphene load at the anti-node and a resonator with two graphene loads situated at opposite ends on the device on the anit-nodes.

7.2.1 Single Graphene Device

A half wave resonator with graphene at an antinode to deliver power to the graphene while minimizing reflections was simulated and fabricated, Figs. 7.2 and 7.3.

The simulated S-parameter data shows resonace is achieved at the designed frequency of 62 GHz, Figs. 7.4-7.6.

Subsequent measurements of the CPW resonator performance were completed at NASA Glenn Research Center. Using a Vector Network Analyzer the S-parameters were collected over the range 57-67 GHz, using GSG probes and calibrated with a CS-5 CPW calibration substrate. Two-port measurements were done on the resonators as well as single port measurements with the opposite port left open. The results of these measurements are displayed in Figs. 7.7-7.9.

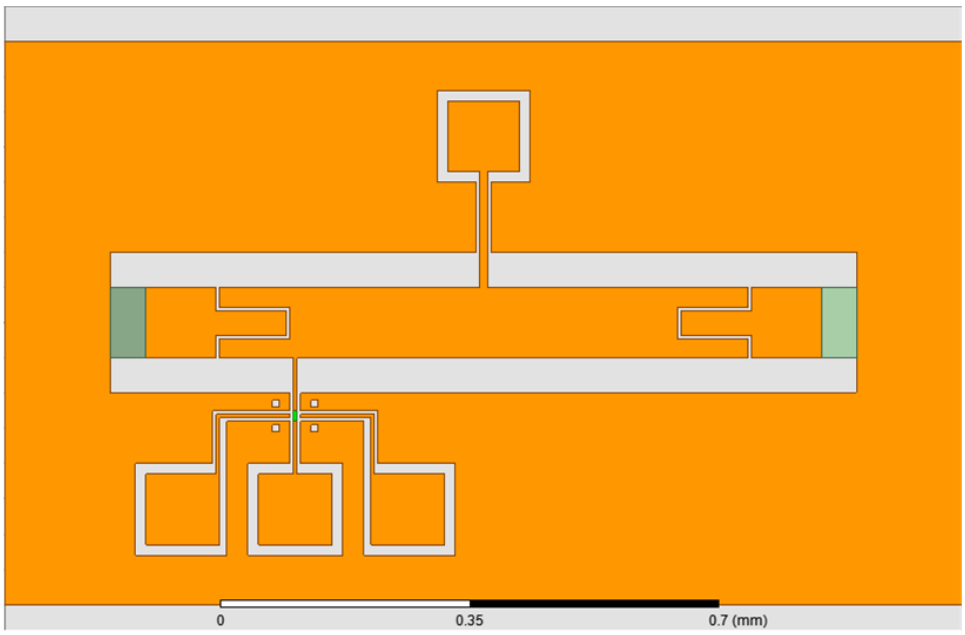

Figure 7.2: Simulated CPW resonator with a single graphene load.

7.2.2 Double Graphene Devices

The second resonator contained two graphene elements, intended to be used for correlation experiments. These structures were simulated and fabricated, Figs. 7.10 and 7.11.

The simulated S-parameter data shows resonace is achieved at the designed frequency of 62 GHz, Figs. 7.12 and 7.13.

Once again, measurements of the CPW resonator performance were completed using a Vector Network Analyzer the s-parameters were collected over the range 57-67 GHz. Two-port measurements were done on both types of resonators

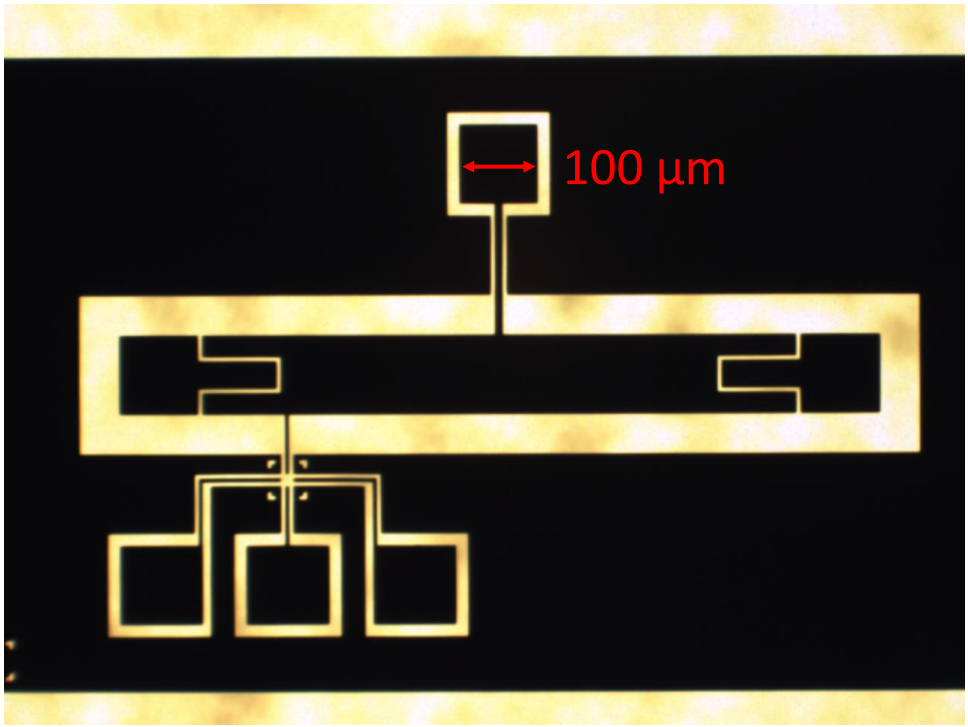

Figure 7.3: Photo of fabricated CPW resonator with a single graphene load.

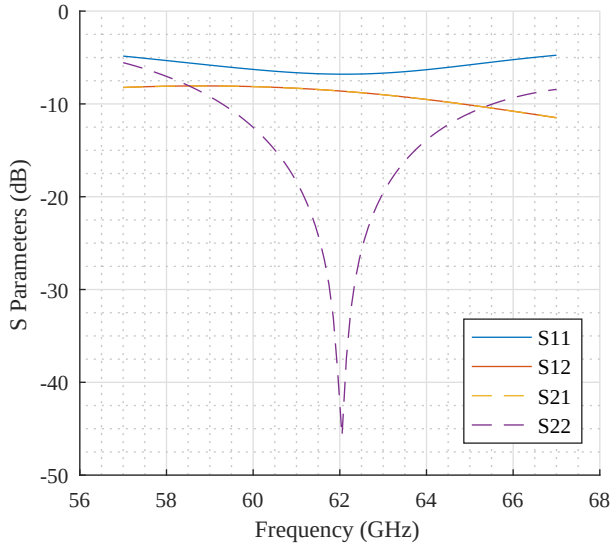

Figure 7.4: Simulated s-paramters of a CPW resonator with a single graphene load.

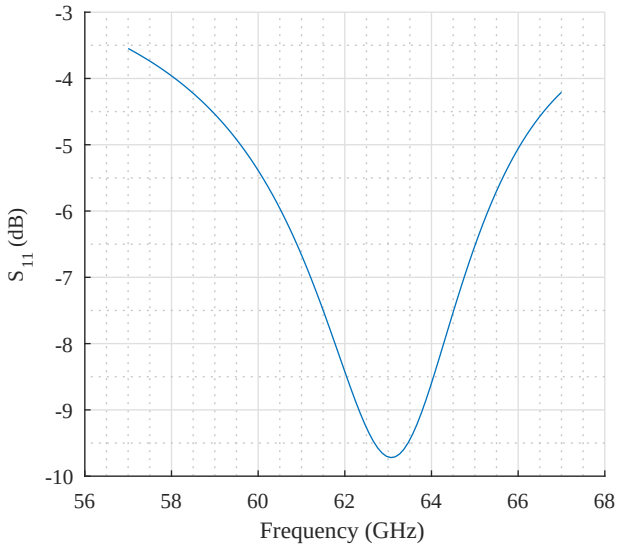

Figure 7.5: Simulated S_{11} of the resonator with port 2 open.

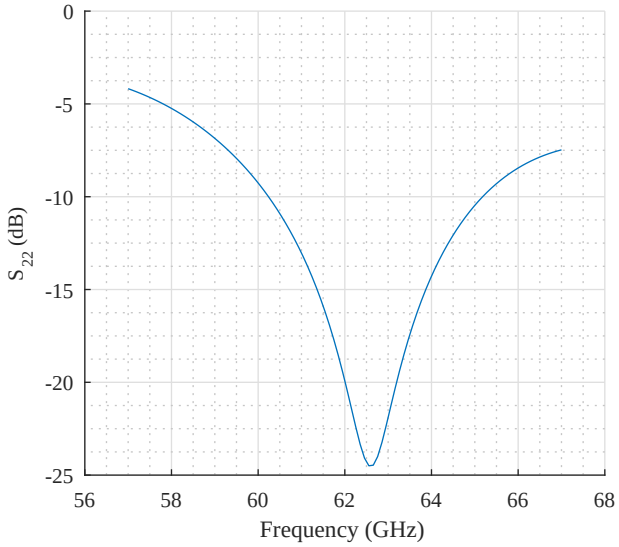

Figure 7.6: Simulated S_{22} of the resonator with port 1 open.

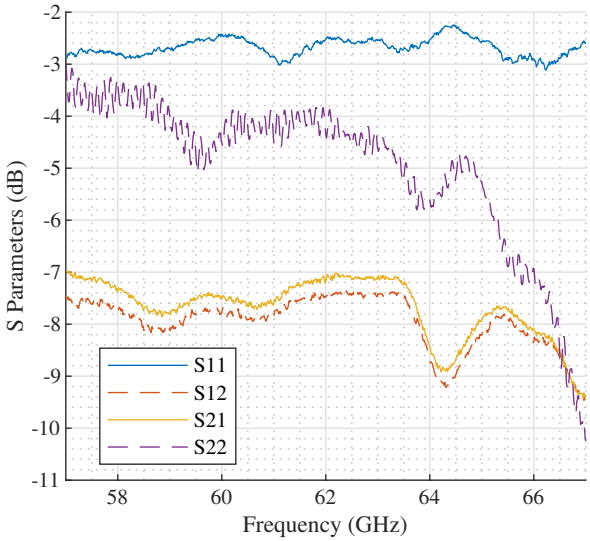

Figure 7.7: Measured s-Parameters of a CPW resonator with a single graphene load.

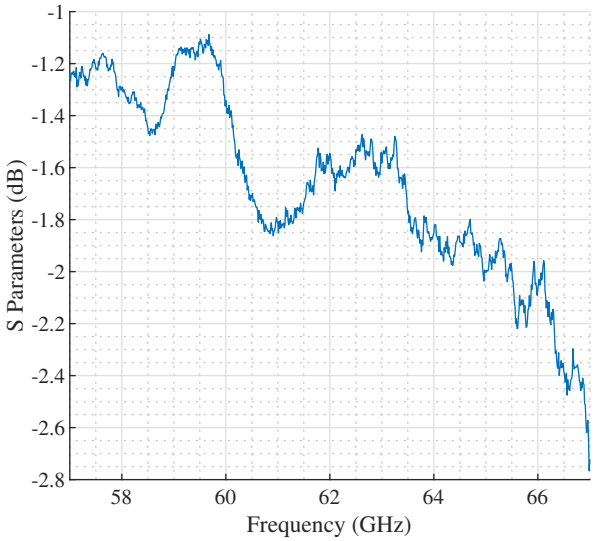

Figure 7.8: Measured reflection coefficient at port 1 of a CPW resonator with port 2 open.

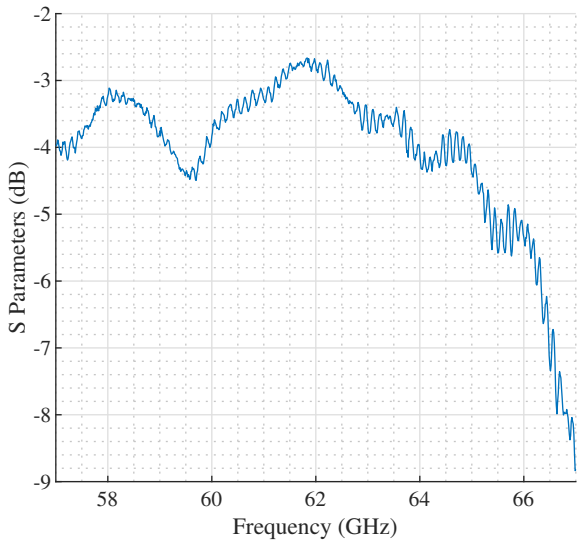

Figure 7.9: Measured reflection coefficient at port 2 of a CPW resonator with port 1 open.

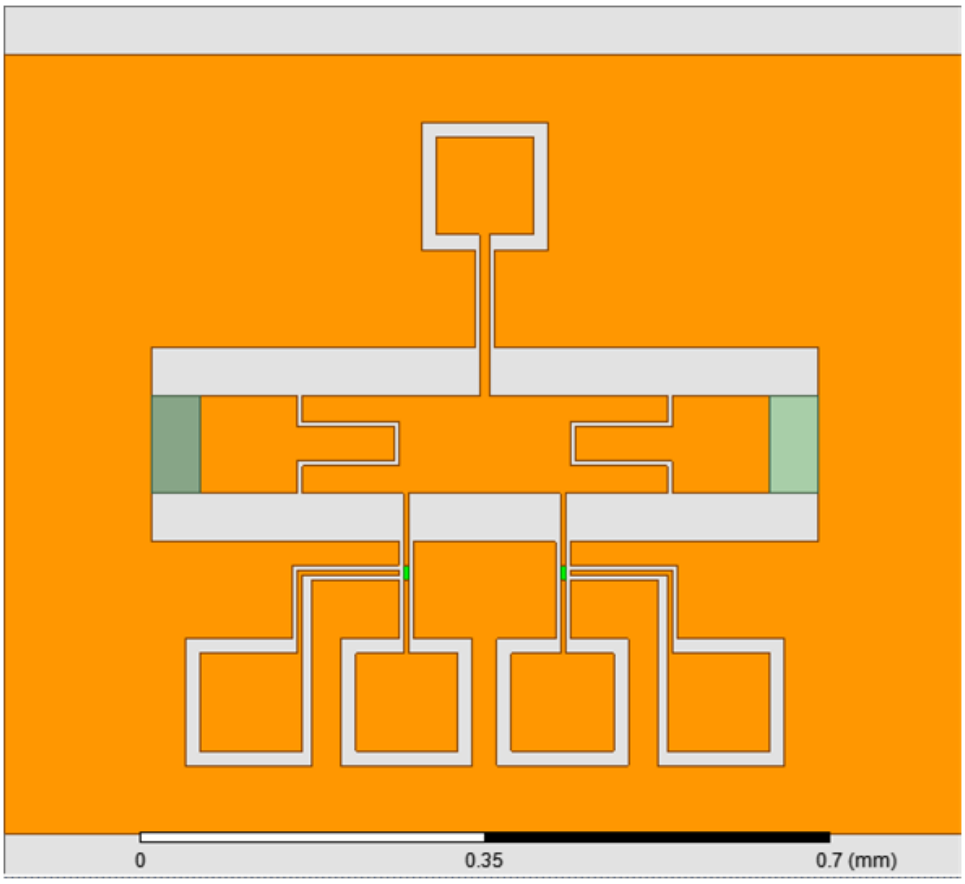

Figure 7.10: Simulated CPW resonator with two graphene loads.

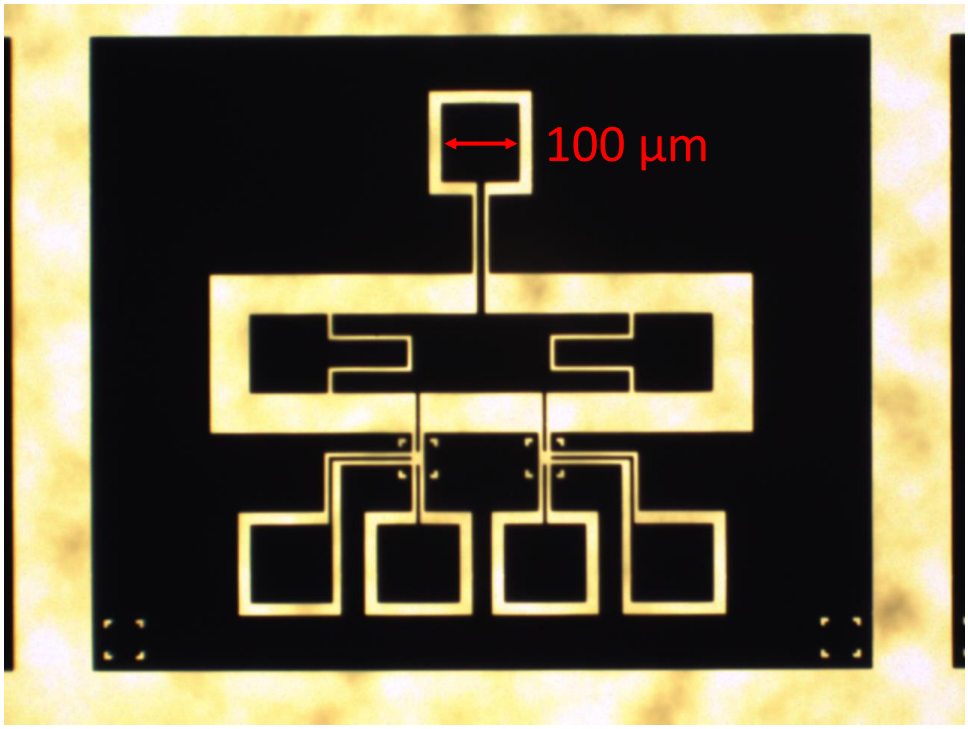

Figure 7.11: Photo of fabricated CPW resonator with two graphene loads.

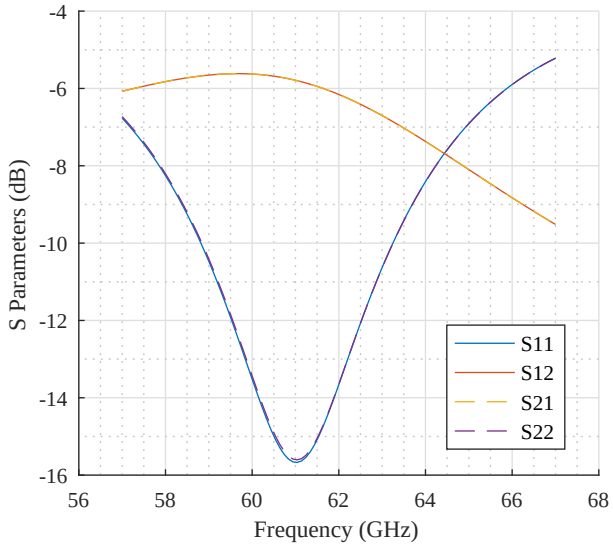

Figure 7.12: Simulated s-paramters of a CPW resonator with two graphene loads.

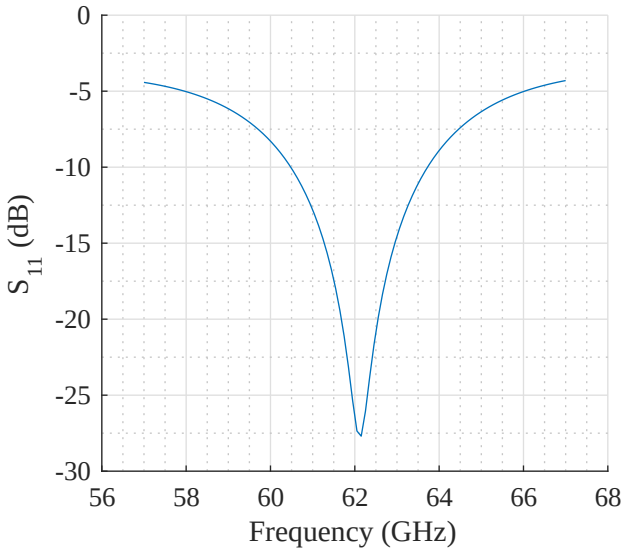

Figure 7.13: Simulated S_{11} (S_{22}) with port 2 (port 1) open.

as well as single port measurements with the opposite port left open. The results of these measurements are displayed in Figs. 7.14-7.16.

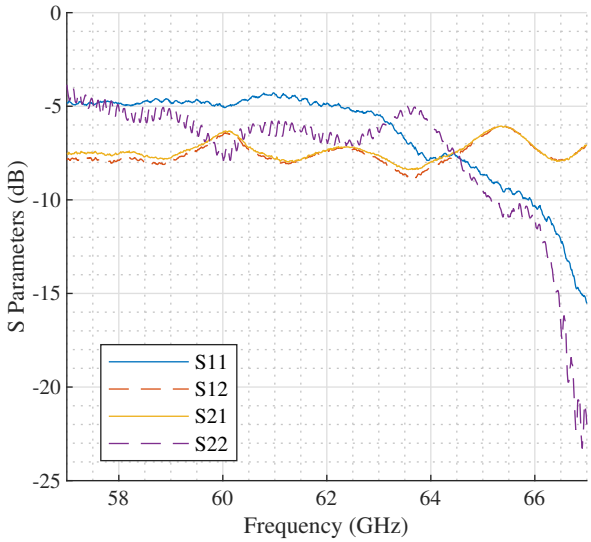

Figure 7.14: CPW resonator with two graphene loads graphene measured S-Parameters.

7.3 Graphene on Sapphire Measurements

Graphene nano-constriction (GNR) devices were fabricated with graphene deposited on a sapphire substrate. These GNRs were identical in dimension to the GNR devices explored in Ch. 6 but included graphene side-gates for conductivity control rather than back-gates. DC characterization was done on the devices, however, many of these devices did not show continuity between the drain and source contacts. Devices that did show electrical continuity displayed poor capacitive coupling at the gate. The

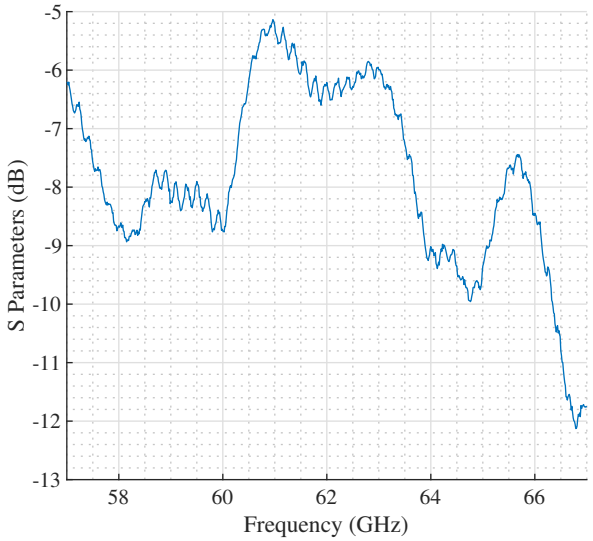

Figure 7.15: CPW resonator with two graphene locations measured port 1 reflection coefficient with port 2 open.

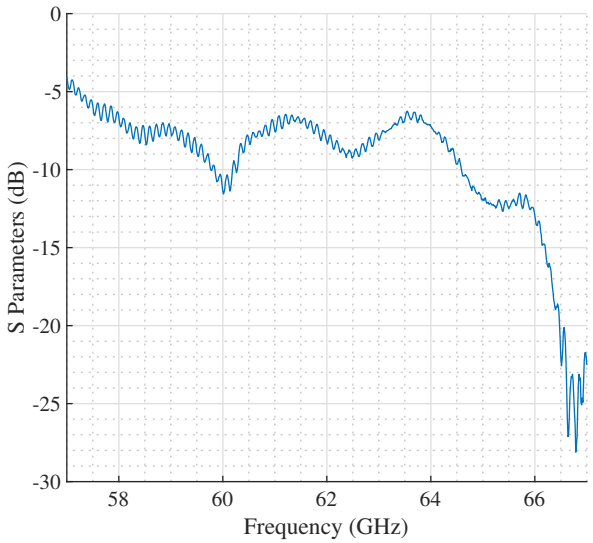

Figure 7.16: CPW resonator with two graphene locations measured port 2 reflection coefficient with port 1 open.

results of two GNR devices with widths of 250 nm are shown in Fig. 7.17. The devices only show a change in drain current on the order to 1-10 μV over an 80 V gate voltage range. The DC curves do not cross the Dirac point. The devices inconsistent values resistance for similar geometries. Due to the nature of the fabrication process and poor electrical performance it is also difficult to determine if the graphene is intact on substrate.

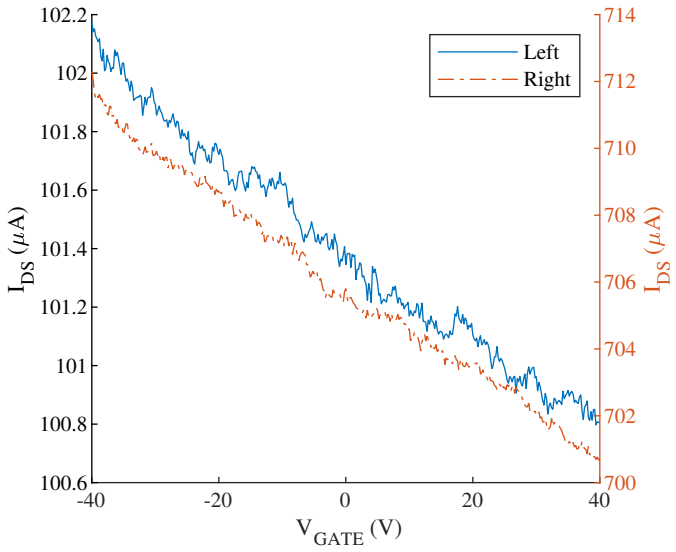

Figure 7.17: Drain-Source conductance as a function of Gate voltage with Drain-Source voltage held at 5 V for two similar devices (left/right).

Improvements can be made on future iterations of these devices. The GNR contriction width could be widened to allow for lower resistance. Future iterations could also include an SiO_2 buffer layer between the sapphire and graphene for improved lattice matching. This would help to prevent delamination and physical

stresses on the graphene layer. Finally, metal side-gate contacts or top-gates could be used instead of graphene side-gates to improve the capacitive coupling at the gate.

7.4 Conclusions

The data collected for the fabricated device does not show a clear resonance at the designed frequency, unlike the simulated device. However, there is a downward trend in the reflection coefficients at the upper frequency limit of 67 GHz. This may indicate that the resonace is beyond the measurement range of the network analyzer and that the simulated relative permittivity of the sapphire did not match the value of the actual substrate. The design of the CPW resonator is very sensitive to the permitivity of the substrate. Measurements on the permittivity of the actual sapphire substrate may be incorporated into the simulation to allow for the resonator dimensions the be reoptimized.

CHAPTER VIII

A GRAPHENE FREQUENCY MULTIPLIER

The goal of this side project is to investigate the non-linear properties of graphene for microwave applications. Specifically, devise a graphene field effect transistor (GFET) to enable frequency multipliers that operate at elevated temperatures and techniques to enable agile/tunable antennas. This research was done in collaboration with personnel from the Communications and Intelligent Systems Division and Facilities Testing Division at NASA Glenn Research Center.

Graphene field effect transistor (GFET) test structures were designed in order to fabricate graphene microwave electronics. Photolithographic techniques were used to fabricate structures for contacting these test structures. Graphene nanostructures were then fabricated using a modified Hitachi scanning electron microscope - specifically a Nabity Pattern Generation System (NPGS) - for direct write E-beam lithography.

Graphene is an excellent choice of material for its versatility in applications. The level of intrinsic carriers in graphene is an order of magnitude less sensitive to temperature than typical semiconductors and the intrinsic mobility is above 100,000 cm^2/Vs at room temperature, making it an ideal candidate for a mission to Venus. Graphene frequency triplers have been demonstrated in previous research [53, 54, 55].

We plan to utilize two series GFETs in a configuration similar to that explored by previous researchers [53].

Graphene can operate over a wide range of temperatures. In addition to the furnace temperatures (up to 500 °C) to be explored for frequency multipliers, prior work with graphene detectors has been done at cryogenic temperatures (down to -193.15 °C). So, the GFETs could offer solutions for lunar mission as the surface temperature of the moon can vary from 123 °C in the day to -153 °C at night.

GFET operation is broadband. Frequency multipliers can be operated over wide range of frequencies, from hundreds of hertz to hundreds of gigahertz [53, 56]. Such wideband operation is of great interest in the field of cognitive communication. A single graphene device has the potential to operate over large bandwidths and a wide range of temperatures. Processing methods developed for the previously described power detectors can be applied to a variety of devices, including these frequency multipliers.

Nonlinear effects seen in semiconductors allow for frequency multiplication. Linear systems do not distort frequency content. Nonlinear systems will introduce higher order harmonics, integer multiples of the fundamental frequency. The Taylor series expansion of an exponential, as in the diode equation, plainly shows this:

$$e^x = 1 + x + \frac{x^2}{2!} + \frac{x^3}{3!} + ... \tag{8.1}$$

It introduces higher order harmics of decreasing intensity as n increases. Graphene can be readily used as a frequency doubler. The "V"-shaped I-V curve

of graphene is very similar to that of a second order polynomial allowing for efficient power transfer into the second harmonic. The goal of the graphene frequency multiplier for a NASA application is to step 10 MHz up to 100 MHz in Venus' atmosphere. Frequency doubling on its own is not enough to achieve this but two frequency triplers can step 10 MHz up to 90 MHz, getting close to the desired frequency. Two series GFETs can alter the characteristic "V"-shaped I-V curve into the "W"-shape seen in Fig. 7. With this DC transfer curve one can observe that when biased properly a third order response can be obtained. Such a response will allow for efficient power transfer into the third harmonic [53, 54, 55].

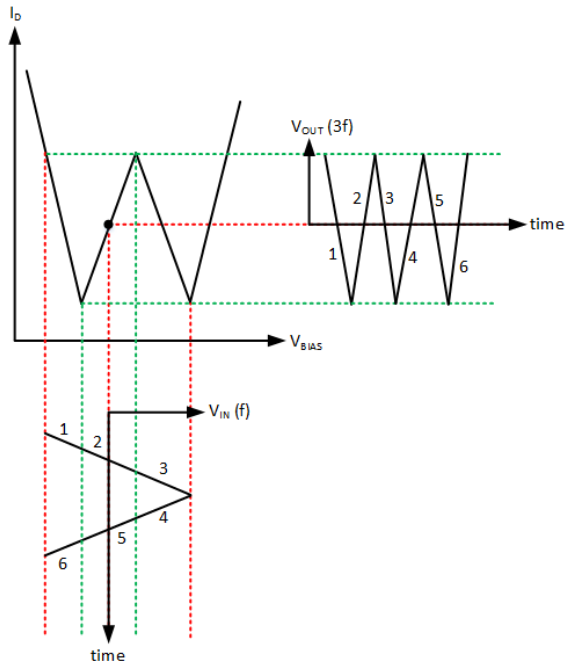

Figure 8.1: Diagram on the operation of a frequency multiplier from two series GFETs with different Dirac points.

Fig. 8.2 shows a schematic and corresponding photograph of the planned series GFET structure. The structure pictured has been fabricated on a silicon substrate. However, silicon is not compatible with Venus' atmosphere and the goal is to fabricate the device on sapphire, Fig. 8.2. However, fabrication on sapphire has proved to be a challenge as dsicussed with regards to the graphene loaded CPW resonators. The photolithographic processes described above are compatible with a sapphire substrate but the electron-beam process must be further optimized in order to obtain a fully functional device.

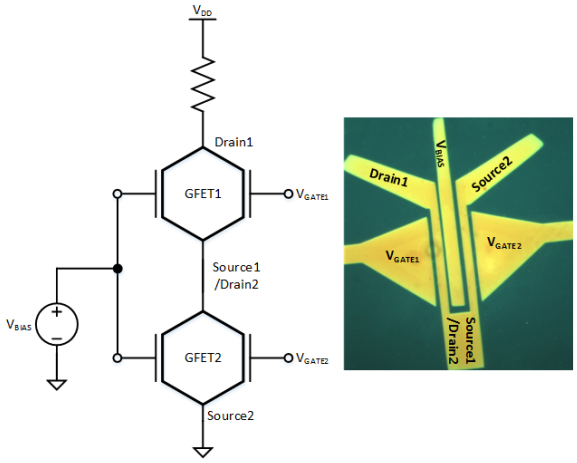

Figure 8.2: Series GFET frequency multiplier schematic and photo.

8.1 Outlook

Using layer and lift-off process we have achieved a micro-device yield up to 95%. An electron-beam lithography process has also been developed for graphene on Si/SiO_2 substrate. Further optimization is needed to utilize sapphire substrates, among other

nonconductive and thermally isolating substrates. Future work will include device measurements once the fabrication process is optimized.

CHAPTER IX

SUMMARY AND CONCLUSIONS

Power detection measurements using graphene Corbino discs yielded a peak power sensitivity of 0.87 mV/mW at room temperature. Device performance was improved through optimizing the fabrication process and device dimensions as well as lowering the operating temperature. Improved micro-structured detectors showed a sensitivity of 3.25 mV/mW at room temperature and 5.44 mV/mW at liquid nitrogen temperature. The simple one mask microfabrication process that was developed has a device yield of 95%. Experimentation then moved towards nano-scaled devices where the final steps in the nanofabrication process reduce this high yield.

Graphene nanoribbon power detector were fabricated and tested that had sensitivities up to 0.14 mV/mW. The nanofabrication process was subsequently improved and microwave power detectors based on GNCs have been demonstrated at room temperature. Results of DC and power detection experiments indicate that the thermoelectric effect is the dominant detection mechanism. The nano-scaled detector had a large reflection coefficient, limiting its power detection capabilities. The GNC detector had a maximum sensitivity of 60.25 mV/mW when accounting for the reflection coefficient. State-of-the-art thermoelectric detectors based on CMOS and MEMS technologies sensitivities are typically lower than 0.4 mV/mW. Without

compensating for signal reflection, the GNR thermoelectric detector yielded a power detection sensitivity of 2.394 mV/mW. This work in the development of graphene power detectors resulted in four publications [16, 23, 32, 38].

A resonator structure was then designed in order to reduce the reflection coefficient of the power detectors and better deliver power to the graphene element. A new fabrication method was developed to realize the structure on a sapphire substrate. However, a mismatch between the simulated and actual value of the substrate permittivity skewed the resonant frequency to a higher value. The design of the resonator may be reoptimized in future work to account for this difference.

Finally, a GFET frequency multiplier structure was designed and fabricated. This device is intended for operation in harsh environments (corrosive atmosphere and high temperature). The fabrication was done using the the developed processes from the power detectors. Testing on this frequency multiplier must be done in the future to ensure that it is capable of operating for extended periods at high temperatures.

BIBLIOGRAPHY

[1] L. Vicarelli, M. S. Vitiello, D. Coquillat, A. Lombardo, A. C. Ferrari, W. Knap, M. Polini, V. Pellegrini, and A. Tredicucci, "Graphene field-effect transistors as room-temperature terahertz detectors," *Nature Materials*, vol. 11, 2012. [Online]. Available: www.nature.com/naturematerials

[2] T. Palacios, A. Hsu, and H. Wang, "Applications of graphene devices in RF communications," *IEEE Communications Magazine*, vol. 48, no. 6, pp. 122–128, June 2010.

[3] F. H. L. Koppens, T. Mueller, P. Avouris, A. C. Ferrari, M. S. Vitiello, and M. Polini, "Photodetectors based on graphene, other two-dimensional materials and hybrid systems," *Nature Nanotechnology*, vol. 9, no. 10, p. 780, 2014.

[4] Wikimedia. Commons. (2010) The ideal crystalline structure of graphene is a hexagonal grid. [Online]. Available: https://https://commons.wikimedia.org/wiki/File:Graphen.jpg

[5] Z. Ni, Y. Wang, T. Yu, and Z. Shen, "Raman spectroscopy and imaging of graphene," *Nano Research*, vol. 1, no. 4, pp. 273–291, 2008.

[6] I. Childres, L. A. Jauregui, W. Park, H. Cao, and Y. P. Chen, "Raman spectroscopy of graphene and related materials," *New Developments in Photon and Materials Research*, vol. 1, 2013.

[7] (2020) Graphenea monloyaer graphene film on various substrates. Graphenea, Inc. [Online]. Available: https://www.graphenea.com/

[8] A. C. Neto, F. Guinea, N. M. Peres, K. S. Novoselov, and A. K. Geim, "The electronic properties of graphene," *Reviews of Modern Physics*, vol. 81, no. 1, p. 109, 2009.

[9] K. S. Novoselov, V. Fal, L. Colombo, P. Gellert, M. Schwab, K. Kim *et al.*, "A roadmap for graphene," *Nature*, vol. 490, no. 7419, p. 192, 2012.

[10] S. Mzali, A. Montanaro, S. Xavier, B. Servet, J.-P. Mazellier, O. Bezencenet, P. Legagneux, M. Piquemal-Banci, R. Galceran, B. Dlubak *et al.*, "Stabilizing a graphene platform toward discrete components," *Applied Physics Letters*, vol. 109, no. 25, p. 253110, 2016.

[11] T. J. Lyon, J. Sichau, A. Dorn, A. Centeno, A. Pesquera, A. Zurutuza, and R. H. Blick, "Probing electron spin resonance in monolayer graphene," *Physical Review Letters*, vol. 119, p. 066802, Aug 2017.

[12] S. Reich, J. Maultzsch, C. Thomsen, and P. Ordejon, "Tight-binding description of graphene," *Physical Review B*, vol. 66, no. 3, p. 035412, 2002.

[13] R. S. Popovic, *Hall Effect Devices Mangnetic Sensors and Characterization of Semiconductors*. IOP Publsihing Ltd, 1991.

[14] R. C. Toonen *et al.*, "Evaluation of carbon nanotube thin films for optically transparent microwave applications using on-wafer probing of corbino disc test structures," ARL, Tech. Rep. 6362, Mar. 2013.

[15] G. Ghione and C. Naldi, "Analytical formulas for coplanar lines in hybrid and monolithic mics," *Electronics Letters*, vol. 20, no. 4, pp. 179–181, February 1984.

[16] M. R. Gasper, N. Parsa, and R. C. Toonen, "Microwave power detection with gated graphene," in *2017 IEEE 17th International Conference on Nanotechnology (IEEE-NANO)*, July 2017, pp. 118–120, ©2017 IEEE. Reprinted, with permission, from M. R. Gasper and N. Parsa and R. C. Toonen.

[17] A. Hsu, H. Wang, K. K. Kim, J. Kong, and T. Palacios, "Impact of graphene interface quality on contact resistance and RF device performance," *IEEE Electron Device Letters*, vol. 32, no. 8, pp. 1008–1010, Aug 2011.

[18] L. G. D. Arco, Y. Zhang, A. Kumar, and C. Zhou, "Synthesis, transfer, and devices of single- and few-layer graphene by chemical vapor deposition," *IEEE Transactions on Nanotechnology*, vol. 8, no. 2, pp. 135–138, March 2009.

[19] K. S. Novoselov, A. K. Geim, S. V. Morozov, D. Jiang, Y. Zhang, S. V. Dubonos, I. V. Grigorieva, and A. A. Firsov, "Electric field effect in atomically thin carbon films," *Science*, vol. 306, no. 5696, pp. 666–669, 2004.

[20] M. R. Gasper, R. C. Toonen, S. G. Hirsch, M. P. Ivill, H. Richter, and R. Sivarajan, "Uncooled radio frequency bolometer based on carbon nanotube thin films," in *2016 IEEE MTT-S International Microwave Symposium (IMS)*, May 2016, pp. 1–4.

[21] ——, "Radio frequency carbon nanotube thin-film bolometer," *IEEE Transactions on Microwave Theory and Techniques*, vol. PP, no. 99, pp. 1–7, 2017.

[22] C. W. Jang, J. H. Kim, J. M. Kim, D. H. Shin, S. Kim, and S.-H. Choi, "Rapid-thermal-annealing surface treatment for restoring the intrinsic properties of graphene field-effect transistors," *Nanotechnology*, vol. 24, no. 40, p. 405301.

[23] M. R. Gasper, R. C. Toonen, N. C. Varaljay, R. R. Romanofsky, and F. A. Miranda, "Microwave power detection with voltage-gated graphene," *IEEE Open Journal of Nanotechnology*, vol. 1, pp. 25–30, 2020, ©2020 IEEE. Reprinted, with permission, from M. R. Gasper and R. C. Toonen and N. C. Varaljay and R. R. Romanofsky and F. A. Miranda.

[24] C. Stellmach, A. Hirsch, G. Nachtwei, Y. B. Vasilyev, N. Kalugin, and G. Hein, "Fast terahertz detectors with spectral tunability based on quantum hall corbino devices," *Applied Physics Letters*, vol. 87, no. 13, p. 133504, 2005.

[25] A. B. Fowler, F. F. Fang, W. E. Howard, and P. J. Stiles, "Magneto-oscillatory conductance in silicon surfaces," *Physical Review Letters*, vol. 16, no. 20, p. 901, 1966.

[26] J. Yan, M. H. Kim, J. A. Elle, A. B. Sushkov, G. S. Jenkins, H.-w. M. Milchberg, M. S. Fuhrer, and H. Drew, "Dual-gated bilayer graphene hot-electron bolometer," *Nature Nanotechnology*, vol. 7, no. 7, pp. 472–478, 2012.

[27] J. A. Robinson, M. LaBella, M. Zhu, M. Hollander, R. Kasarda, Z. Hughes, K. Trumbull, R. Cavalero, and D. Snyder, "Contacting graphene," *Applied Physics Letters*, vol. 98, no. 5, p. 053103, 2011.

[28] "Peak values of conductivity in integer and fractional quantum hall effect," *Solid State Communications*, vol. 96, no. 5, pp. 309–312, 1995.

[29] T. Ihn, *Semiconductor Nanostructures: Quantum states and electronic transport*. Oxford University Press, 2010.

[30] S. Cristoloveanu, T. V. C. Rao, Q. T. Nguyen, J. Antoszewski, H. Hovel, P. Gentil, and L. Faraone, "The corbino pseudo-mosfet on soi: Measurements, model, and applications," *IEEE Transactions on Electron Devices*, vol. 56, no. 3, pp. 474–482, March 2009.

[31] K. Ziegler, "Minimal conductivity of graphene: Nonuniversal values from the kubo formula," *Physical Review B*, vol. 75, no. 23, p. 233407, 2007.

[32] M. R. Gasper, R. C. Toonen, N. C. Varaljay, R. R. Romanofsky, and F. A. Miranda, "Nanoscale fabrication of microwave detectors from commercially-available cvd-grown monolayer graphene," in *2018 IEEE 13th Nanotechnology Materials and Devices Conference (NMDC)*, Oct 2018, pp. 1–4, ©2018 IEEE. Reprinted, with permission, from M. R. Gasper and R. C. Toonen and N. C. Varaljay and R. R. Romanofsky and F. A. Miranda.

[33] M. Y. Han, B. Özyilmaz, Y. Zhang, and P. Kim, "Energy band-gap engineering of graphene nanoribbons," *Physical Review Letters*, vol. 98, p. 206805, May 2007.

[34] E. Herth, E. Algre, P. Tilmant, M. Francois, C. Boyaval, and B. Legrand, "Performances of the negative tone resist aznlof 2020 for nanotechnology applications," *IEEE Transactions on Nanotechnology*, vol. 11, no. 4, pp. 854–859, 2012.

[35] B. R. Romanczyk, *Fabrication and characterization of III-V tunnel field-effect transistors for low voltage logic applications.* Rochester Institute of Technology, 2013.

[36] S. Kumar, N. Peltekis, K. Lee, H.-Y. Kim, and G. S. Duesberg, "Reliable processing of graphene using metal etchmasks," *Nanoscale Research Letters*, vol. 6, no. 1, p. 390, May 2011.

[37] J.-W. Kim, Y.-C. Kim, and W.-J. Lee, "Reactive ion etching mechanism of plasma enhanced chemically vapor deposited aluminum oxide film in cf4/o2 plasma," *Journal of Applied Physics*, vol. 78, no. 3, pp. 2045–2049, 1995.

[38] M. R. Gasper, R. C. Toonen, N. C. Varaljay, R. R. Romanofsky, and F. A. Miranda, "Thermoelectric graphene nano-constrictions as detectors of microwave signals," *IEEE Transactions on Nanotechnology*, vol. 18, pp. 879–884, 2019, ©2019 IEEE. Reprinted, with permission, from M. R. Gasper and R. C. Toonen and N. C. Varaljay and R. R. Romanofsky and F. A. Miranda.

[39] F. Xia, T. Mueller, Y.-m. Lin, A. Valdes-Garcia, and P. Avouris, "Ultrafast graphene photodetector," *Nature Nanotechnology*, vol. 4, no. 12, p. 839, 2009.

[40] T. Mueller, F. Xia, and P. Avouris, "Graphene photodetectors for high-speed optical communications," *Nature Photonics*, vol. 4, no. 5, p. 297, 2010.

[41] D. Yi, X. Wei, and Y. Xu, "Transparent microwave absorber based on patterned graphene: Design, measurement, and enhancement," *IEEE Transactions on Nanotechnology*, vol. 16, no. 3, pp. 484–490, May 2017.

[42] M. Jung, P. Rickhaus, S. Zihlmann, P. Makk, and C. Schönenberger, "Microwave photodetection in an ultraclean suspended bilayer graphene p–n junction," *Nano Letters*, vol. 16, no. 11, pp. 6988–6993, 2016, pMID: 27704863.

[43] V. Milanovic, M. Gaitan, E. D. Bowen, N. H. Tea, and M. E. Zaghloul, "Thermoelectric power sensor for microwave applications by commercial cmos fabrication," *IEEE Electron Device Letters*, vol. 18, no. 9, pp. 450–452, Sep. 1997.

[44] D. Wang, X. Liao, and T. Liu, "A thermoelectric power sensor and its package based on mems technology," *Journal of Microelectromechanical Systems*, vol. 21, no. 1, pp. 121–131, Feb 2012.

[45] Z. Zhang, Y. Guo, F. Li, Y. Gong, and X. Liao, "A sandwich-type thermoelectric microwave power sensor for GaAs MMIC-compatible applications," *IEEE Electron Device Letters*, vol. 37, no. 12, pp. 1639–1641, Dec 2016.

[46] Z. Zhang and X. Liao, "Characteristics of doped n+GaAs thermopile-based RF MEMS power sensors for MMIC applications," *IEEE Electron Device Letters*, vol. 38, no. 10, pp. 1473–1476, Oct 2017.

[47] A. S. Brush, "Measurement of microwave power - a review of techniques used for measurement of high-frequency RF power," *IEEE Instrumentation Measurement Magazine*, vol. 10, no. 2, pp. 20–25, April 2007.

[48] C. W. Jang, J. H. Kim, J. M. Kim, D. H. Shin, S. Kim, and S.-H. Choi, "Rapid-thermal-annealing surface treatment for restoring the intrinsic properties of graphene field-effect transistors," *Nanotechnology*, vol. 24, no. 40, p. 405301, 2013.

[49] W. K. Kim, J. Oh, H. S. Yoon, S. J. Kim, J. Y. Park, J. Jung, and S. Chan Jun, "Impedance variation on lattice misoriented few-layer graphene via layer decoupling," *IEEE Transactions on Nanotechnology*, vol. 18, pp. 55–61, 2019.

[50] Y. M. Zuev, W. Chang, and P. Kim, "Thermoelectric and magnetothermoelectric transport measurements of graphene," *Physical Review Letters*, vol. 102, p. 096807, Mar 2009.

[51] T. Mueller, F. Xia, M. Freitag, J. Tsang, and P. Avouris, "Role of contacts in graphene transistors: A scanning photocurrent study," *Physical Review B*, vol. 79, p. 245430, Jun 2009.

[52] "Zero Biased Detector With 50 Ohm SMA Male to SMA Female Video Out Operating From 10 MHz to 2 GHz Configuration Bias Type Zero Biased Detector Detector Polarity Negative Body Style Straight RF Input Connector SMA Male RF Input Impedance 50 Ohms Video Output," Tech. Rep., 2013. [Online]. Available: www.Pasternack.com

[53] H.-Y. Chen and J. Appenzeller, "Graphene-based frequency tripler," *Nano Letters*, vol. 12, no. 4, pp. 2067–2070, 2012, pMID: 22452648.

[54] C. Cheng, B. Huang, J. Liu, Z. Zhang, X. Mao, P. Xue, and H. Chen, "A pure frequency tripler based on cvd graphene," *IEEE Electron Device Letters*, vol. 37, no. 6, pp. 785–788, June 2016.

[55] P. Peng, Z. Tian, M. Li, Z. Wang, L. Ren, and Y. Fu, "Frequency multiplier based on back-gated graphene fets with m-shaped resistance characteristics," *Journal of Applied Physics*, vol. 125, no. 6, p. 064503, 2019.

[56] S. Ver Hoeye, A. Hadarig, C. Vázquez, M. Fernández, L. Alonso, and F. Las Heras, "Submillimeter wave high order frequency multiplier based on graphene," *IEEE Access*, vol. 7, pp. 26 933–26 940, 2019.

APPENDICES

APPENDIX A

DETAILS ON THE MICROFABRICATION OF GRAPHENE CORBINO DISCS

This process is in reference to the fabrication of graphene micro-devices. The sample is a 1 cm $\times$ 1 cm chip graphene on Si/SiO_2 or sapphire. It is the goal of this appendix to read as a set of instructions in order to aid in the recreation or expansion on this work.

The Rapid Thermal Anneal and Passivation

A rapid thermal anneal is first done to clean the sample. The RTA is done in Forming Gas (a mixture of Nitrogen and Hydrogen) at 250 °C for 12 minutes. The samples are then immediately passivated with 2.5 nm of Aluminum. Note: aluminum thicknesses may vary but 2.5 nm was found to offer adequate protection while still being easily removable.

Removing Back Oxide

This step is only necessary for Si/SiO_2 samples that have an oxide layer on the back. Newer samples provided by graphenea should not have this oxide layer.

1. **Clean**: Soak the sample in heated (55 °C) acetone for approximately 30 minutes. Spray with acetone, dry with N_2, Spray with IPA, then dry with N_2.

2. **Spin**: Spin on the positive tone photoresist AZ4210. Ramp up spin at 500 rpm for 3 seconds followed by 3000 rpm for 47 seconds.

3. **Bake**: Place the in an overn at 95 °C for 30 minutes.

4. **Acid Etch**: Soak in 1:1::dH_2O:(6:1 BOE) for 6 minutes, rinse with dH_2O (under faucet) for 2 minutes, then dry with N_2.

Graphene Patching

These steps detail the process for creating patches of graphene from a chip that is blanket coated with passivated graphene. The patches allow for device isolation and better metal adhesion onto parts of the substrate rather than entirely on the graphene.

1. **Clean**: Overnight soak in acetone (approx. 20 hours), spray with acetone, dry with N_2, spray with IPA, then dry with N_2.

2. **Spin**: Spin on the photoresist AZ5214-E IR. Ramp up spin at 500 rpm for 3 seconds followed by 4000 rpm for 42 seconds.

3. **Edge-Bead Removal**: Done with Napkin Point using AZ EBR.

4. **Pre-Exposure Bake**: Place the sample on at hotplate at 90 °C for 3 minutes. Let cool for approx. 60 seconds.

5. **Exposure**: Done with MJB-3 unit.Power set to 275 W on Ch 1. Mask used: Gasper_CorbinoPatch_Aug2018 (-PR). Exposure done for 20 seconds with intensity of 15.1 mW/cm^2.

6. **Development**: Develop in AZ300 MIF for 30 seconds. Rinse in DI water for 5 seconds and soak in a separate DI water for at least 60 seconds. Note: 30 seconds may be too long for 2.5 nm Al.

7. **Reactive Ion Etch**: March RIE (used Recipe 5 O_2/Ar) 20% O_2, 50% Ar, 60 seconds, 100 W.

8. **PR Strip**: Soak the sample in heated (55 °C) acetone for approximately 30 minutes. Spray with acetone, dry with N_2, Spray with IPA, then dry with N_2.

Device Patterning

These steps detail the process of patterning device contacts on a substrate. Two types of photoresist are considered. AZ nLOF2020 for thin metal structures ($< 1\mu$m) and AZ nLOF2070 for thick metal structures ($> 1\mu$m). The thin process was used in this work on Si/SiO_2 substrates, while the thick metal process was used on sapphire substrates.

Thin Metal Process:

1. **Clean**: Overnight soak in acetone (approx. 1 hours), spray with acetone, dry with N_2, spray with IPA, then dry with N_2.

2. **Spin**: Spin on AZ nLOF2020 mixutre, 1:1 (by weight) with AZ EBR. Ramp up spin at 500 rpm for 3 seconds followed by 4000 rpm for 42 seconds.

3. **Edge-Bead Removal**: Done with Napkin Point using AZ EBR.

4. **Bake**: Place the sample on at hotplate at 110 °C for 60 seconds.

5. **Exposure**: Done with MJB-3 unit.Power set to 275 W on Ch 1. Exposure done for 1.5 seconds with intensity of 15.1 mW/cm^2.

6. **Post Exposure Bake**: Place the sample on at hotplate at 110 °C for 60 seconds.

7. **Development**: Develop, no agitation, in AZ300 MIF for 30 seconds. Rinse in DI water for 5 seconds and soak in a separate DI water for at least 60 seconds.

8. **Metallization**: In E-beam evaporator, deposit 5 nm Cr and 50 nm Au.

9. **Lift-off**: Soaked in Remover PG heated to 70 °C for approx. 1 hour. Agitate with pipet. Spray with IPA and dry with N_2.

Note: Diluted AZ nLOF2020 may be spinning on too thin. Consider using undiluted.

Thick Metal Process:

1. **Clean**: Overnight soak in acetone (approx. 1 hours), spray with acetone, dry with N_2, spray with IPA, then dry with N_2.

2. **Spin**: Spin on AZ Electronic Grade Adhesion Promoter. Ramp up spin at 500 rpm for 3 seconds followed by 3000 rpm for 55 seconds.

3. **Bake**: Place the sample on at hotplate at 180 °C for 8 minutes.

4. **Spin**: Spin on AZ nLOF2070. Ramp up spin at 500 rpm for 3 seconds followed by 7000 rpm for 55 seconds.

5. **Edge-Bead Removal**: Done with Napkin Point using AZ EBR, only on the corners.

6. **Bake**: Place the sample on at hotplate at 110 °C for 90 seconds.

7. **Exposure**: Done with MJB-3 unit.Power set to 275 W on Ch 1. Exposure done for 3.5 seconds with intensity of 15 mW/cm^2.

8. **Post Exposure Bake**: Place the sample on at hotplate at 110 °C for 60 seconds.

9. **Development**: Develop, no agitation, in AZ300 MIF for 30 seconds. Rinse in DI water for 5 seconds and soak in a separate DI water for at least 60 seconds (repeat one time).

10. **Metallization**: In E-beam evaporator, deposit 50 nm Ti and 3 μm layer of (Au).

11. **Lift-off**: Soaked in Remover PG heated to 70 °C for approx. 1 hour. Agitate with pipet. Spray with IPA and dry with N_2.

APPENDIX B

DETAILS ON THE NANOFABRICATION OF GRAPHENE STRUCTURES

This process is in reference to the fabrication of graphene nano structures. The sample is a 1 cm $\times$ 1 cm chip of graphene on Si/SiO_2 or sapphire. This process may take upwards on 7 or more hours depending on the number and complexity of structures to be written. The SEM used is a Hitachi S2460N modified with a Nabity Nano Pattern Generation System. It is the goal of this appendix to read as a set of instructions in order to aid in the recreation or expansion on this work.

Before any nanofabrication: make sure that the SEM stage is in a known position over a gold standard or Faraday cup. This is to ensure that when the SEM is powered on that the beam will hit some area of the stage and not the sample and avoid unecessary exposure of the sample. Steps noted with a (*) are done only when using non-conductive substrates.

Sample Preparation

1. **Clean**: The sample was cleaned blow blowing the sample with nitrogen. It was placed on a hotplate at 180 °C for 3 minutes. It was then allowed to cool on a room temperature aluminum plate for 3 minutes.

2. **Spin**: The resist used is Dow Corning XR-1541 006 (HSQ). Apply approximately 5 drops of resist on the sample from a clean pipet, and dispose of the pipet after use (**DO NOT REUSE PIPETS WITH HSQ**). Ramp up spin at 500 rpm for 3 seconds followed by 5000 rpm for 42 seconds.

3. **Pre-Exposure Bake**: Place the sample on at hotplate at 80 °C for 4 minutes for Si/SiO_2 (90 °C for 3 minutes for sapphire).

4. ***Spin**: PEDOT:PSS conductive polymer. Coat the sample using a clean pipet. Ramp up spin at 500 rpm for 5 seconds followed by 5000 rpm for 55 seconds.

5. **Load the SEM**: Place the sample on the SEM stage and clip it at one corner. Place the stage and sample in the SEM and begin chamber evacuation.

SEM Beam Optimization

Proper SEM beam optimization is critical in E beam writing to ensure that the beam is well focused and thermally stable.

1. **Set Working Distance**: Set a working distance (WD) of approximately 12 mm. The resolution of the working distance on the S2460N is not precise. Adjust the WD to 11 mm and slowly increase it until it switches over to 12 mm.

2. **Set Accelerating Voltage**: Turn the SEM on and turn the voltage up to 20 kV. Once at 20 kV slowly increase the voltage to 30 kV. If arcing is heard while increasing the voltage, then turn off the beam and examine the system.

3. **Set Beam Current**: Slowly turn up the beam current until it reaches a saturation point. Measure the beam current with the faraday cup and adjust the current until it measures 10 pA is reached.

4. **Beam Equilibration**: Allow the SEM to thermally equilibrate for at least 30 minutes. The beam current can drift 10-20% in this time.

5. **Reset Beam Current**: Use the fine adjustment knob to reset the current to 10 pA, measured with the Faraday cup.

6. **Focus**: Adjust focus

7. **Astigmatism**: Adjust astigmatism

After optimizing the beam, avoid readjusting the focus or astigmatism settings. Control focus from this point on using the Z-axis control micrometer of the SEM stage.

Exposure and Development

1. **Exposure**: The optimal dose was found to be 200 μC/cm^2. Use NPGS for exposure and stage control.

2. **Remove Sample**: After exposure, return the stage to a known position. Slowly turn the beam current to zero. Slowly return the accelerating voltage to zero and turn off the beam. Purge the chamber and remove the sample.

3. ***Development**: Submerge the sample in a heated DI water bath for 60 seconds to remove the PEDOT:PSS.

4. **Development**: Develop in AZ300 MIF for 4 minutes. Rinse in DI water for 5 seconds and soak in a separate DI water for at least 60 seconds.

Areas of HSQ exposed to the electron beam are hardened into a glass-like material and cannot be removed at this point. This layer will act as a etch stop to pattern the graphene in a reactive ion etch.